Mechanism and kinetics of the thermal decomposition of $Fe(C_5H_5)_2$ in inert and reductive atmosphere: A synchrotron-assisted investigation in a microreactor

Sebastian Grimm[a,c]*, *Patrick Hemberger*[b], *Tina Kasper*[c,d], *Burak Atakan*[a,d]

[a] IVG, Institute for Combustion and Gas Dynamics – Mass Spectrometry in Reacting Flows, University of Duisburg-Essen, 47057, Germany
[b] Laboratory for Synchrotron Radiation and Femtochemistry, Paul Scherrer Institute, CH-5232 Villigen-PSI, Switzerland
[c] IVG, Institute for Combustion and Gas Dynamics – Mass Spectrometry in Reacting Flows, University of Duisburg-Essen, 47057, Germany
[d] CENIDE, Center for Nanointegration Duisburg-Essen, University of Duisburg-Essen, 47057, Germany

E-mail address: sebastian.grimm@uni-due.de (S. Grimm)

Keywords: photoelectron photoion coincidence spectroscopy; pyrolysis; ferrocene; metallocene; kinetics

The decomposition and reduction of ferrocene, an important precursor for iron CVD and catalyst for nanotube synthesis, was investigated with a versatile and sensitive experimental method. The gas-phase reactive intermediates are detected to understand the underlying chemistry by using a microreactor coupled to a synchrotron light source. Utilizing soft photoionization coupled with photoelectron-photoion coincidence detection enables to characterize elusive intermediates isomer-selectively. We propose a reaction mechanism for the ferrocene decomposition, which proceeds as a two-step process. Initially, the molecule decomposes in a homogeneous surface reaction at temperatures < 900 K, leading to products such as cyclopentadiene and cyclopentadienyl radicals that are immediately released to the gas-phase. At higher temperatures, ferrocene rapidly decomposes in the gas-phase, losing two cyclopentadienyl radicals in conjunction with iron. The addition of hydrogen to the reaction mixture reduces the decomposition temperature, and changes the branching ratio of the products. This change is mainly attributed to the H-addition of cyclopentadienyl radicals on the surface, which leads to a release of cyclopentadiene into the gas-phase. On the surface, ligand fragments may also undergo a series of catalytic H-losses leading most probably to a high

carbon content in the film. Finally, Arrhenius parameters for both global reactions are presented.

1. Introduction

Since its discovery in the 1950's,[1,2] the metallocene ferrocene ($Fe(Cp)_2$), is, due to its remarkable stability[3], an extensively studied compound.[4] It is a classical sandwich complex, where two cyclopentadienyl ligands are attached to a central iron core. Ferrocene is characterized by a relatively high vapor pressure at moderate temperatures, it is non-toxic and stable in air and therefore an easy to handle precursor for the synthesis of functional materials.[5] In particular, the use of ferrocene has been successfully established in the preparation of iron-containing thin films for optoelectronic devices[6,7] or iron thin films in oxidative atmosphere in metallurgical applications.[8] Upon thermal decomposition of $Fe(Cp)_2$, iron nanoparticles (Fe-NP) can be formed which may subsequently act as functional nanomaterials for energy conversion and storage systems.[9,10] Those Fe-NPs have additionally shown excellent performance and emission characteristics in biodiesel engines[11,12] and as a burning catalyst in rocket propellants[13], since hydrocarbon radicals, responsible for soot formation, are quenched.[11] Nowadays, ferrocene is among the most widely used precursors in the synthesis of carbon nanotubes (CNTs),[14] either as a feedstock to produce catalytic sites necessary for their growth,[15–22] or as both carbon and catalyst precursor.[23–26] Those functional nanomaterials are often manufactured by high yield, low temperature methods,[14] as for instance by catalytic chemical vapor deposition (CCVD). The underlying synthesis routes and processes were extensively studied experimentally[15–17,19,20,27–29] and numerically.[30–35] It can be concluded, that the hydrocarbon source has a major influence on the morphology, crystallinity and growth kinetics of CNTs, mediated through its gas-phase decomposition products pertaining to its initial structure,[36] as well as the catalyst activity. The control of product quality requires understanding the gas-phase decomposition mechanism of ferrocene at various reaction conditions. The intermediates act either as promoter of CNT growth by serving as carbon feedstock or as detrimental impurity, lowering the growth rate by forming unwanted volatile and polyaromatic hydrocarbons,[37,38] deactivating the iron catalyst particles by forming Fe_3C (cementite), or by carbon incorporation or encapsulation.[8] Consequently, vast research has been conducted on the decomposition products[25,39,40] and kinetics,[41] experimentally and by molecular dynamic simulations.[42] The latter suggest that the bonds in the ferrocene molecule break above 1073 K sequentially according to bond strength: C—H > C—C > Fe—C. The formation of cyclopentadienyl radicals (C_5H_5) was observed experimentally by mass spectrometry[39,41] and infrared laser pyrolysis.[40] Dyagileva et al.[41] conducted a kinetic study on the pyrolysis of ferrocene in closed glass vessels under vacuum by the manometric method and concluded that the solid decomposition products, namely carbon

and iron, catalyze the decomposition by a factor of almost 3000 lowering the decomposition onset temperature to 823 K. They proposed first order reaction conditions with a rate constant of $1.6 \cdot 10^{-5}$ s^{-1} at 823 K. Main products formed are H_2, CH_4, C_2H_6 and C_2H_4 in the static system analyzed by electron ionization mass spectrometry, whereas no radicals or elusive species were observable in a continuous flow reactor. This may be due to the rather long residence times. Gas-phase iron nanoparticles were also not observed in this study.[41] In a later study, also cyclopentadiene and ethylene (C_2H_4) were observed at temperatures starting from 873 K, which may also originate from reactions catalyzed by chemisorbed iron atoms on the surface, which explains the low decomposition temperature.[43] These studies come to the conclusion that most of the species detected are either formed in the secondary decomposition of cyclopentadiene (C_5H_6) to methane and hydrogen, or in catalytic reactions on the wall.[41] Ensuring homogenous conditions by infrared laser pyrolysis, Russel et al.[40] studied the gas-phase pyrolysis of ferrocene and observed C_5H_6, C_5H_5 and naphthalene ($C_{10}H_8$) among the decomposition products and proposed reaction schemes for their formation. Nevertheless, those products are partially secondary products and owing to the detection method used, no short-lived iron species could be detected either, rendering the decomposition mechanism to be still elusive.[40]

In earlier investigations it was observed that adding hydrogen to the carrier gas stream has a beneficial outcome regarding catalyst lifetime because H_2 acts as a reductive agent,[33,44] and allows a control of the amount of desired carbon product formed.[45] H_2 is also reported to lead to a significantly lower decomposition temperature of ferrocene.[6,35,46]

Recently, we demonstrated that vacuum ultraviolet (VUV) synchrotron radiation coupled with a vacuum flash pyrolysis microreactor and photoelectron photoion coincidence (i^2PEPICO)[47] detection can be used to unravel the gas-phase chemistry decomposition of CVD precursors.[48] Thanks to the tunability of the photon energy together with velocity map imaging (VMI), we were able to distinguish fragmentation and direct ionization and thus identify important organometallic and organic reactive intermediates isomer-selectively to elucidate the underlying chemistry. Here, we report a detailed VUV-i^2PEPICO study for the in-situ detection of gas-phase radicals and molecular iron during pyrolysis of $Fe(C_5H_5)_2$ at conditions relevant to CCVD and CNT growth. To investigate the influence of hydrogen on the reaction mechanism of $Fe(C_5H_5)_2$ 10% H_2 was added to the mixture before entering the reaction zone. Our results provide direct experimental evidence for initial steps of the $Fe(C_5H_5)_2$ reaction steps through a detailed analysis of the gas-phase composition. It can be used to improve simulation efforts of CNT as well as thin film growth and hencecontribute to more efficient material synthesis.

2. Results and Discussion

A pyrolysis microreactor coupled to a molecular beam source, where reactive species are not quenched, is coupled to the photoelectron photoion coincidence spectrometer. Intermediates and products are detected by mass spectrometry and photoion mass-selective threshold photoelectron spectra (ms-TPES). Furthermore, dissociative photoionization is distinguished from direct ionization of reactive species, which allows to extract unimolecular decomposition pathways of ferrocene in an inert as well as in hydrogen atmosphere. Finally, we investigate the reaction kinetics in terms of activation energy and rate coefficients for the global reactions observed in the experiment, based on a numerical simulation of the flow field.

2.1 Dissociative photoionization of ferrocene: Does $Fe(C_5H_5)^+$ (*m/z* 121) form in the gas-phase ?

As outlined in the introduction, many published reaction schemes propose the formation of $Fe(C_5H_5)$ as initial product in the gas-phase, whereas none of these studies detected the molecule experimentally. A possible reason could be that, experimental limitations or fragmentation interfered with the results. Since our system is capable of detecting elusive species, as for instance $Fe(C_5H_5)$, its detection appears feasible.[48,49]

When dealing with the detection of reactive radicals in ionization processes, fragment ions from dissociative photoionization (DPI) of the precursor needs to be distinguished from direct ionization of the radical in the hot reactor. From the literature[50] we know, that ferrocene (*m/z* 186) loses a cyclopentadienyl (C_5H_5) ligand upon DPI at a 0 K appearance energy of 13.16 eV[51] according to:

$$Fe(C_5H_5)_2 + h\nu \rightarrow Fe(C_5H_5)^+ + C_5H_5 + e^- \quad (1)$$

In order to understand this process, we heated up the reactor to 1079 K and followed the *m/z* 121 signal as a function of the photon energy. The threshold photoelectron spectrum (ms-TPES) and the photoion efficiency curve (PIE) of *m/z* 121 are depicted in **Figure 1 (a)**. We clearly observe an increase in the relative intensity of the signal at 11.1 eV, but find some signal already at around 9.6 eV. Ionization energy calculation at different levels of theory for the $Fe(C_5H_5)$ find values of 6.45 (B3LYP/6-311+G++(d,p)), 6.66 (ωB987xd/6-311+G++(d,p)) and 6.13 eV M06L/6-311+G++(d,p)), respectively, which are much lower than the observed ionization onset. The signal increase at 9.6 eV in the PIE/ ms-TPES can thus not be rationalized with direct ionization. On the other hand, the

onset is also too low as compared to the literature dissociative ionization threshold of 13.1 eV. Instead, the reason for the signal increase at lower photon energy, than the value reported in the literature, is the high internal energy of the neutral molecule due to heating of the gas in the reactor.[52] This can shift the onset of the dissociative ionization to lower photon energies in the ms-TPE spectrum (**Figure 1 (a)**, green curve) and was observed in the literature before using the similar reactors.[52,53] Another indication for DPI is an asymmetric peak shape of the TOF distribution in the mass spectra, caused by a slow unimolecular dissociation, which takes place upon acceleration of the ion in the mass spectrometer and was also observed for the peak at *m/z* 121.[54] Additionally, our experimental apparatus enables us to unambiguously observe ion fragmentation thanks to the velocity map imaging (VMI) technique. Here the DPI can be clearly identified as a broad translational energy distribution of the fragments perpendicular to the molecular beam as shown in **Figure 1(b)**. This is characteristic for dissociative ionization of the neutral molecule (see **Figure 1 (b)**, "beam"), if compared[55,56] to a molecular beam resulting from direct ionization as shown in the supplemental material on **Figure S1**. Thus, we conclude that the signal of $Fe(C_5H_5)$ is caused by dissociative rather than direct ionization. As a consequence, we cannot confirm the gas-phase formation of this species, which contradicts the literature mechanisms, which proposes $Fe(C_5H_5)$ to be the major initial decomposition product in the gas-phase.[25,34,40] Nevertheless, we cannot exclude that $Fe(C_5H_5)$ is formed and decomposes further or immediately adsorbs on the reactor

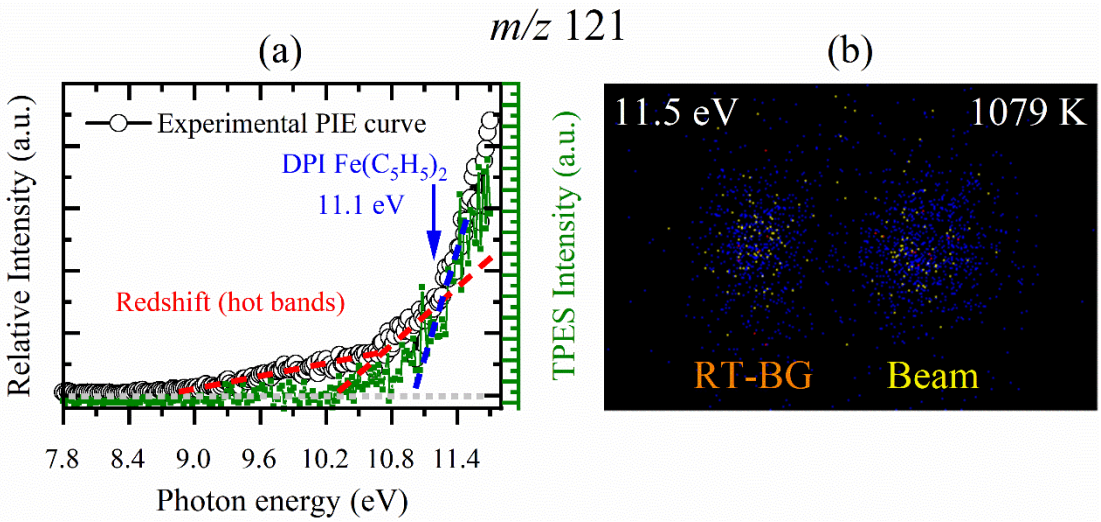

Figure 1 (a) Experimental PIE curve and ms-TPES of *m/z* 121 at 1079 K. The contribution of thermal energy to the internal energy of the ion leads to a red shift in ionization energy to lower values (red curves); the appearance energy of $Fe(C_5H_5)^+$ has been determined to be 11.1 eV (blue curve). **(b)** Ion momentum image (VMI) of *m/z* 121 at 1079 K, which shows the kinetic energy distribution of the ions that reach the ion detector. A part of the excess energy of photoionization is released as kinetic energy, which results in a broad velocity distribution of the room-temperature background (orange) and the beam component (yellow). This enables us to distinguish between direct and dissociative photoionization of the neutral molecule. For comparison, a focused molecular beam of direct ionization is shown in **Figure S1** of the **ESI**.

wall, where it may react at higher temperatures due to homogeneous or heterogeneous surface reactions. This possibility will be discussed later in this manuscript.

2.2 Photoionization mass spectra

After we successfully distinguished signals associated with dissociative from direct ionization of pyrolysis products, only product signals that emanate from pyrolysis are discussed in the following. Photoionization mass spectra were recorded and evaluated at fixed photon energies of 9.0, 10.5, and 11.5 eV over a temperature range of 333-1250 K. **Figure 2** illustrates exemplary mass spectra of the pyrolysis products at fixed photon energies of 9.0, and 11.5 eV with and without (top trace) pyrolysis. When the SiC-reactor is heated, we clearly see a depletion of the precursor`s ion signal at *m/z* 186. Product peaks at *m/z* 65, 66, 80 and 128 are observed in the mass spectra at temperatures above 781 K (**Figure 2 (left)**) at slightly lower temperature thresholds than reported in the literature, where no decomposition for the low pressure pyrolysis was observed up to 1178 K.[57] These peaks grow in intensity when the temperature is further increased, together with a decline of the *m/z* 186 parent ion signal. The first iron containing signal at *m/z* 56 is detected at temperatures > 1087 K. Additionally, some

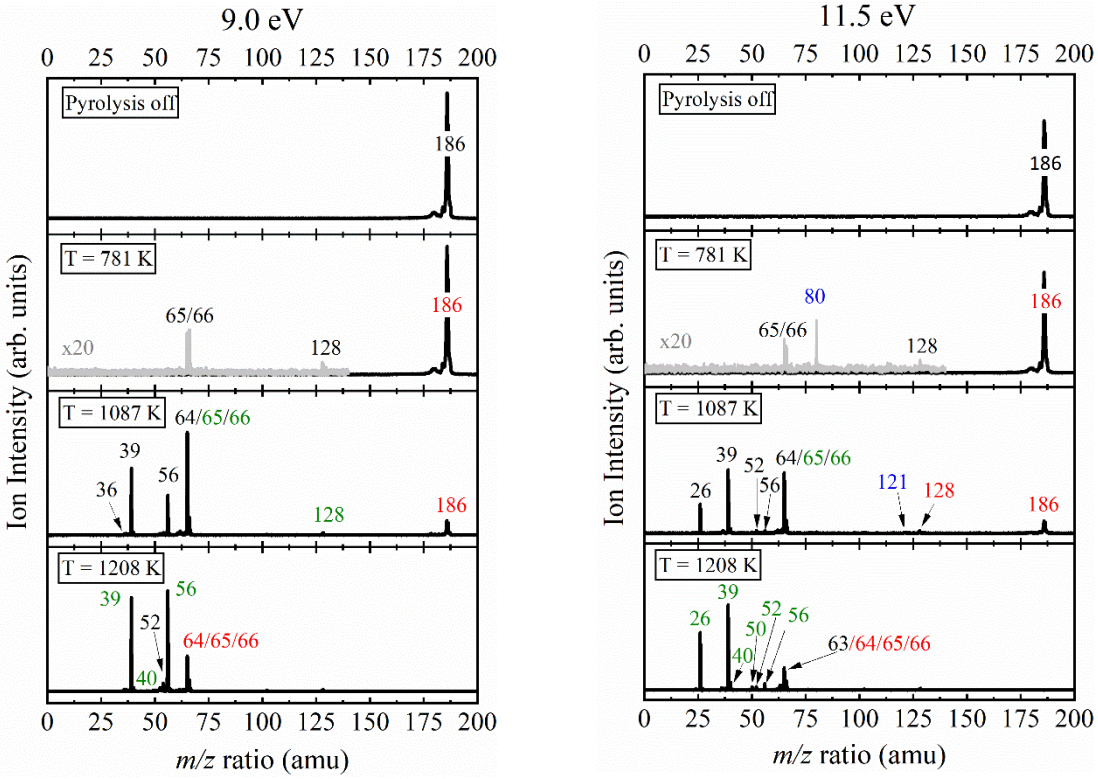

Figure 2 Temperature-dependent mass spectra of $Fe(C_5H_5)_2$ pyrolysis recorded at a photon energy of 9.0 (**left**) and 11.5 eV (**right**) and an inlet mole fraction of 8.2 x 10^{-4} (0.08 %). The major peaks are assigned by their *m/z* ratio and with respect to their absolute decay (red) or increase (green) in comparison to the previous spectrum at lower decomposition temperature. Species that emerge for the first time are marked in black color, whereas the blue numbers indicate that the species are due to dissociative ionization or impurities. For better comparison, the gray spectra are multiplied by a factor of 20.

new product peaks arise in the spectrum at *m/z* 39, 52 and 64, which are most likely secondary decomposition products of the initially observed hydrocarbons at lower temperatures. To assess product species with lower masses or larger ionization energy onsets, mass spectra at higher photon energies were recorded (**Figure 2 (b)**). At temperatures above 1200 K, several peaks appear at *m/z* ratio < 70, while the primary decomposition product signal at *m/z* 65 decreases markedly. In addition to the previously noticed peaks in the literature[40,41,57], our mass spectra show evidence of species with *m/z* 26, 39, 40 and 52 upon depletion of the primary decomposition product *m/z* 65, whose origin has not yet been clarified.

The peak at *m/z* 80 is assigned to cyclopentadienone (see **Figure 2**), which may result from traces of oxygen in the reaction mixtures. Because no oxygen flow was intentionally added in our experiments, it is considered an impurity, as will be discussed briefly in the **ESI Figure S2**.

2.3 Identification of elusive species

Photoion mass-selected threshold photoelectron spectroscopy (ms-TPES) is an indispensable tool for the isomer-selectivity detection of reactive species in pyrolysis, combustion, and catalysis if experimental data is compared to literature or Franck-Condon simulated spectra.[55,58] To understand the underlying chemistry of $Fe(C_5H_5)_2$ pyrolysis we plotted a threshold photoionization matrix (TPM) at a reactor temperature of 1117 K as partially shown in **Figure 3 (a)**.[59] In this presentation our multidimensional data set is reduced to a photon energy and mass spectrometric axis, while the threshold photoelectron signal intensities correspond to a change in color from light blue to red. By analyzing this illustration, the mass channels, where the main pyrolysis products reside, can be identified. If we extract the data along a horizontal line for a given mass, ms-TPE spectra can be derived, and it is possible to characterize the major pyrolysis species for each *m/z* ratio. Exemplary spectra of the most abundant species obtained this way are shown in subfigures **(b)**, **(c)** and in **Figure 4**. We can clearly identify strong signals at *m/z* 26, 39, 56, 65, 66. So far the coexistence of Fe and C_5H_5 as the most abundant products upon pyrolysis was only hypothetical.[57] Clear onsets at 7.98 and 8.88 eV in the TPES of *m/z* 56, which corresponds to the published $^6D \leftarrow ^5D$ and $^4D \leftarrow ^5D$ transition of iron (7.90 and 8.89 eV,[60] see **Figure 3 (b)**), confirms this observation. The analysis of the spectrum in **Figure 3 (c)** additionally shows, that the cyclopentadienyl radical

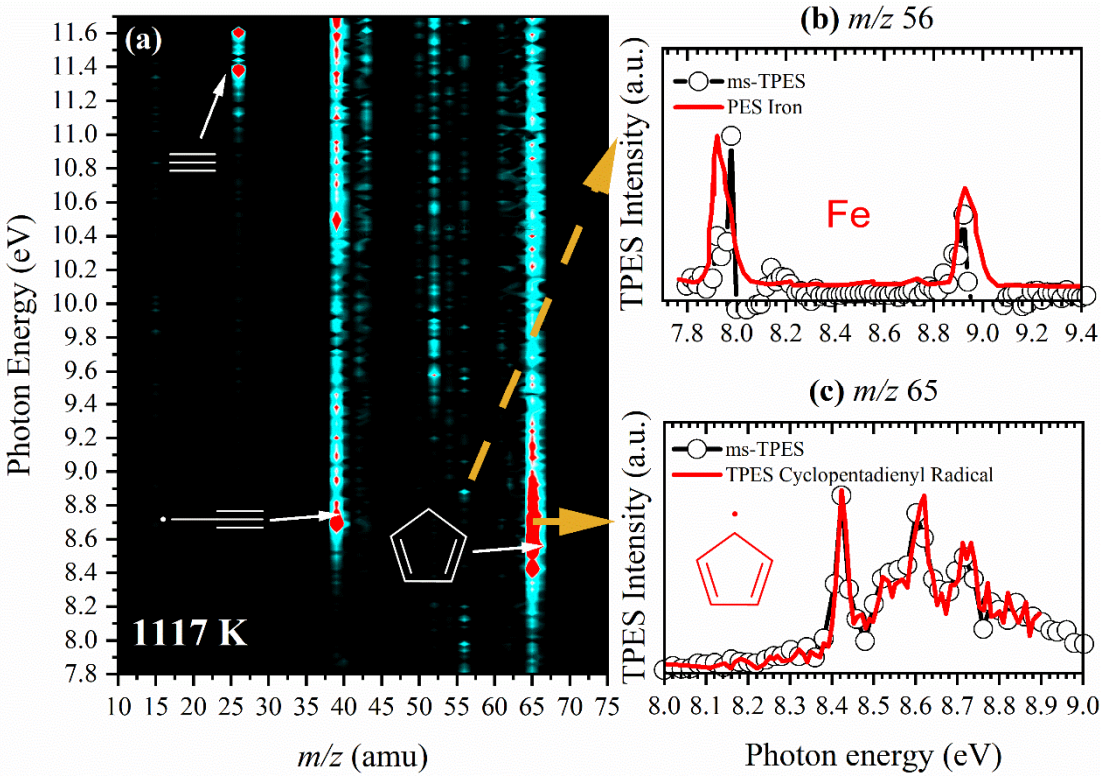

Figure 3 (a) Threshold photoionization matrix (TPM) for the identification of the major decomposition products. The subgraphs are representative vertical samples from the TPM at **(b)** *m/z* 56 and **(c)** *m/z* 65. Iron[60] and the cyclopentadienyl radical[61] were unambiguously identified by literature reference spectra (red). Additional identified products are denoted by their chemical structure in white and their characterization is further discussed in the text.

is the most abundant pyrolysis product, which contributes to the *m/z* 65 signal (IE = 8.42 eV)[61] . The onset of the TPE spectrum of *m/z* 26 at 11.39 eV in **Figure 4 (a)** fits the literature spectrum of acetylene (C_2H_2) (IE = 11.4 eV)[62] well. At 8.7 eV a peak in the TPE spectrum of *m/z* 39 emerges and can clearly be assigned to the propargyl radical (C_3H_3) with a vertical IE = 8.71 eV[63] (see **Figure 4 (b)**). The majority of the TPE signal at *m/z* 66 in **Figure 4 (c)** matches a strong transition of cyclopentadiene (c-C_5H_6) with an ionization energy of 8.57 eV,[64] whereas also contributions of the acyclic isomer 1,2,4-pentatriene at 8.70 eV[65] may be identified. Because of the large internal energy of the neutrals, hot bands are responsible for a signal level that is non-zero below the actual ionization onset. Due to the vibrational progression of the ground state band of cyclopentadiene and the limited signal-to-noise ratio (SNR), traces of other isomers with *m/z* 66 with higher ionization energies are, if present, difficult to characterize. In **Figure 4 (d)** we have also plotted the excited station spectrum of ferrocene between 8 and 10 eV. Note that the ionization energy is 6.71eV.[66]

In **Figure 5**, a collection of the most important minor product species are shown. The TPE-spectrum with *m/z* 50 in **Figure 5 (a)** fits the literature photoelectron spectrum of 1,3- butadiyne at IE = 10.17 eV[67] well and is solely assigned to this isomer of C_4H_2. The majority of the signal at *m/z* 52 in panel **(Figure 5 (b))** is ascribed to vinylacetylene (1-butene-3-yne) by a strong band

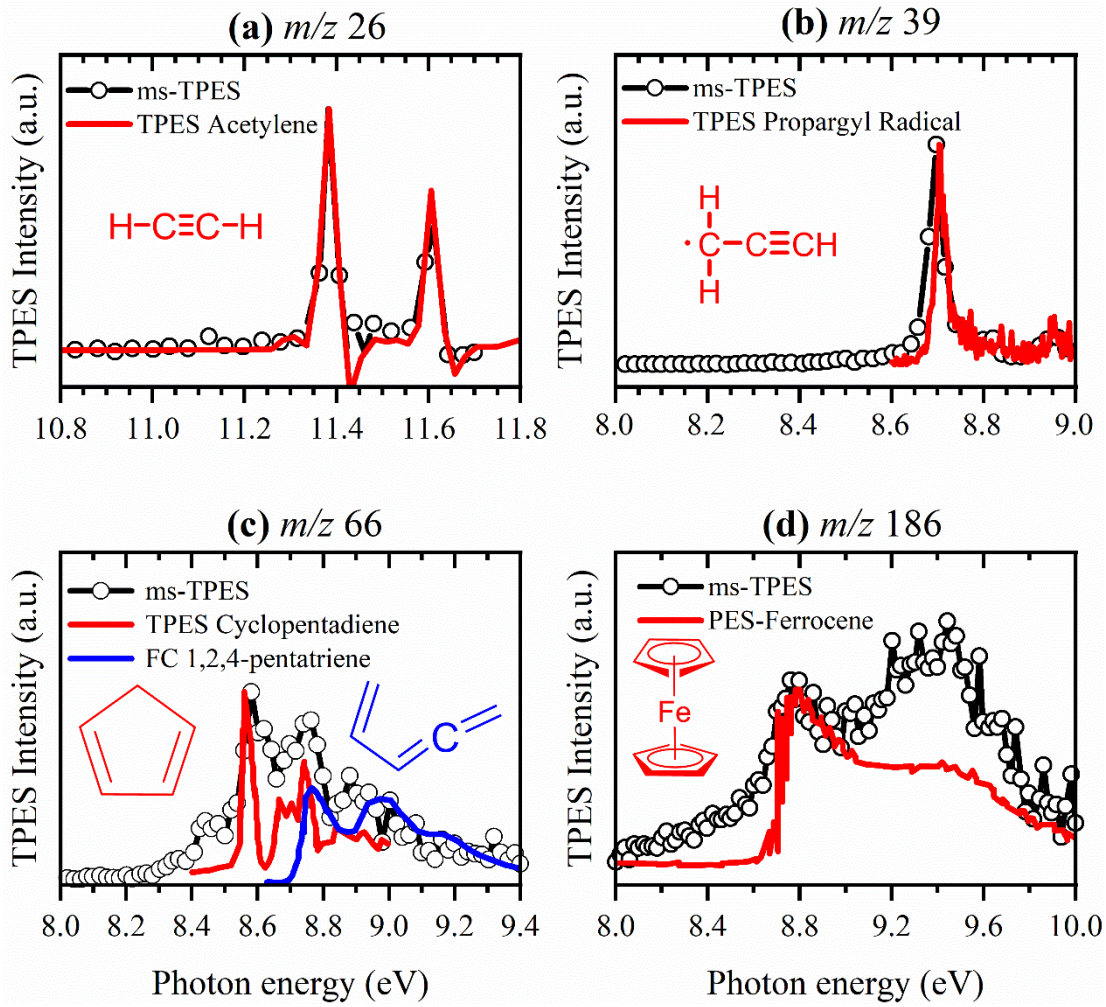

Figure 4 Representative examples of species identification and assignment of major species using experimental obtained TPE (black dots and lines); species are either characterized by literature reference spectra (red), or by computed spectra (blue) in **(a)-(d)**. References are as follows: **(a)** *m/z* 26 C_2H_2,[62] **(b)** *m/z* 39 C_3H_3,[63] **(c)** *m/z*.66 c-C_5H_6[64] and 1,2,4-pentatriene,[65] **(d)** *m/z* 186 Fe(C_5H_5).[80]

at its IE = 9.58 eV.[68] The ms-TPE spectrum in **Figure 5 (c)** at *m/z* 64 gives evidence, that cyclic, as well as non-cyclic C_5H_4 species are present in the sample. Given the ionization energies of 8.42 and 8.67 eV for c-C_5H_4,[69] it is tempting to assign the signal to the cyclopentadienylide carbenes, however the peaks coincide with transitions of the cyclopentadienyl radical and are results of mass separation in the ms-TPES. We can however find contributions of the acyclic isomer 1,3 pentadiyne represented by 9.50 eV.[70] Interestingly, also larger hydrocarbons were identified in the spectra at *m/z* 128 shown in **Figure 5 (d).** Here, traces of naphthalene were identified by a small signal increase around 8.16 eV that fits the contour of the literature TPE spectrum, with an IE of 8.14 eV.[71] Here, the comparison with Frank-Condon simulations obtained from Pan et al.[72] revealed, that 3-butene-1-ynylbenzene with an IE at 8.74 eV explains the majority of the TPE signal in **Figure 5 (d),** whereas a small contribution of 1-butene-3-ynylbenzene (IE= 8.53 eV) is identified. Besides these assignments,

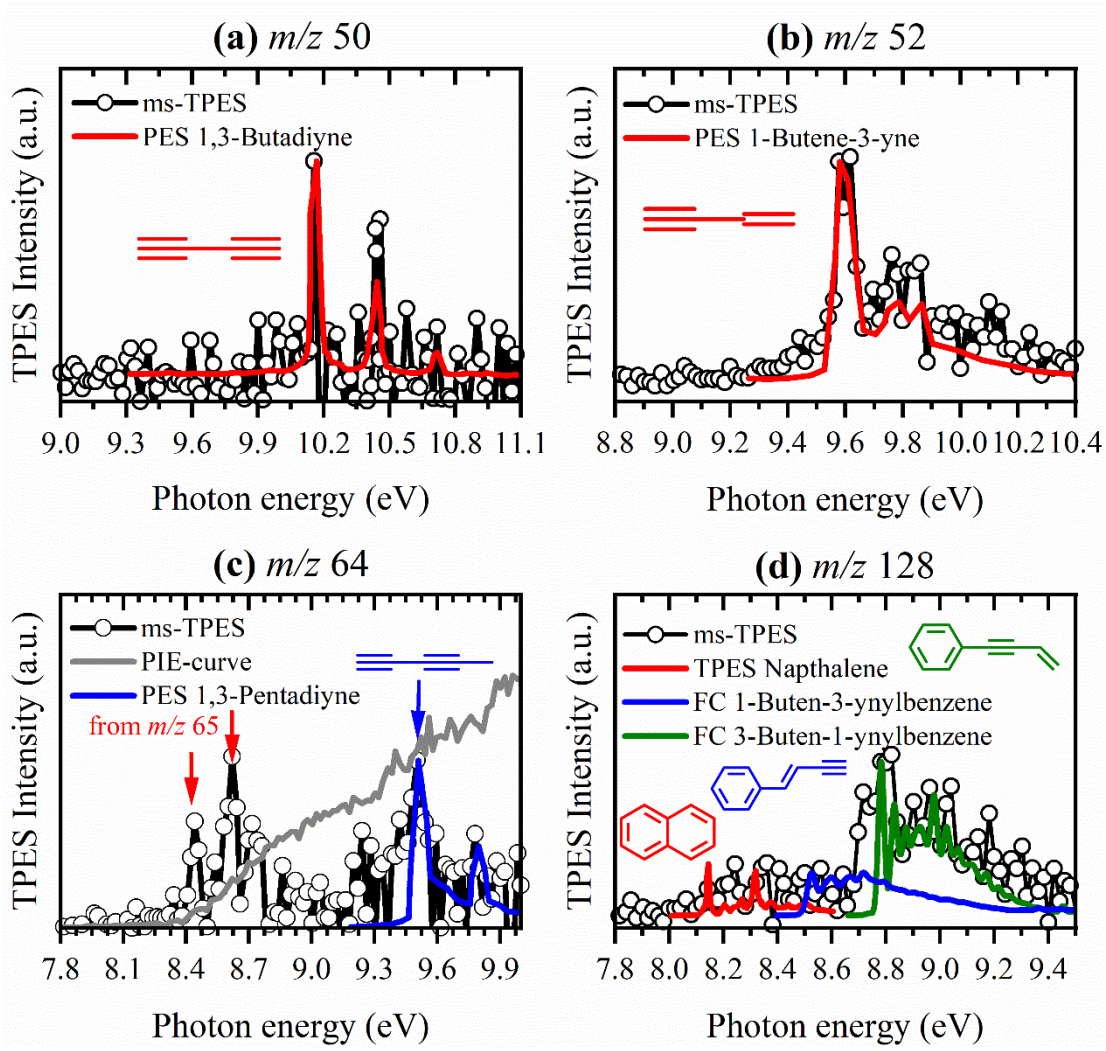

Figure 5 Representative examples of species identification and assignment of the minor decomposition products using experimental obtained TPE spectra (black dots and lines); species are either characterized by literature reference spectra (red) in **(a)-(d)**, by specific ionization onsets in the gray PIE-curve **(c)** or Frank-Condon simulations (FC) in **(d)**. References are as follows: **(a)** *m/z* 50 C_4H_2[67], **(b)** *m/z* 52 C_4H_2 red: vinylacetylene (1-butene-3-yne)[68] **(c)** *m/z*.64 red: contributions from *m/z* 65, blue: 1,3 pentadiyne;[70] **(d)** *m/z* 128 red: naphthalene,[71] blue: 1-buten-3-ynylbenze,[72] green: 3-Buten-1-ynylbenzene.[72]

5 other products were identified by comparison between the ms-TPES and literature data, whenever accessible and are summarized in **Table 1.** Noting that the sample is highly diluted and only small amounts of the minor products were identified, they are not considered in the major thermal-decomposition pathways, as discussed later in the text.

Table 1: List of identified species upon pyrolysis of $Fe(C_5H_5)_2$ and the reduction with H_2 (marked with asterisk) by VUV-i^{2}PEPICO using their adiabatic and vertical ionization energies. Reference spectra and energies have been taken from the literature and are denoted at the respective value. The identification of the compounds in bold are discussed further in the paper.

			IE [eV]
m/z	Formula	Name	Reference
15	CH_3	Methyl radical	9.84[73]
24	C_2	Dicarbon	-
26	**C_2H_2**	**Acetylene**	**11.4**[62]
36	C_3	Tricarbon	-
39	**C_3H_3**	**Propargyl radical**	**8.71**[63]
40	C_3H_4	Allene	9.69[74]
		Propyne	10.38[75]
42*	**C_3H_6**	**Propene**	**9.73**[76]
43*	**C_3H_7**	**i-Propyl radical$^+$**	**n.a.**
		n-Propyl radical$^+$	**n.a.**
44*	**C_3H_8**	**Propane**	**10.9**[76]
50	**C_4H_2**	**1,3-Butadiyne**	**10.17**[67]
52	**C_4H_4**	**1-Buten-3-yne**	**9.58**[68]
54*	C_4H_6	1,3-butadiene	9.07[77]
		2-butyne	9.59[76]
		1-butyne	10.18[66]
56	**Fe**	**Atomic iron (^{6}D←^{5}D); (^{4}D←^{5}D)**	**7.90; 8.89**[60]
64	**C_5H_4**	**Ethynylallene**	**9.22**[69]
		1,3-Pentadiyne	**9.50**[70]
65	**C_5H_5**	**Cyclopentadienyl radical**	**8.41**[61]
66	**C_5H_6**	**1,3-cyclopentadiene**	**8.58**[64]
		1,2,4-pentatriene	**8.70**[65]
80	C_5H_4O	2,4-Cyclopentadiene-1-one (impurity) (see **S2** in **ESI**)	9.42[78]
128	**$C_{10}H_8$**	**Naphthalene**	**8.14**[71]
		1-butene-3-ynylbenzene	**8.53**[72]

		3-butene-1-ynylbenzene	**8.74**[72]
186	**$Fe(C_5H_5)_2$**	**Ferrocene (excited state band)**	**6.9, (8.4-8.7)**[79]

2.4 Pyrolysis pathways of ferrocene

The pyrolysis reaction pathways are temperature-dependent so that a measurement of all decomposition products and intermediates at different temperatures are needed to deduce the overall reaction scheme. The temperature-dependent ion signals of the most important intermediates are shown in **Figure 6**. Based on the unambiguous species assignments in **Figure 3, 4** and **5** and mechanistic considerations from the species profiles from **Figure 6**, we describe the predominant pathways for the pyrolysis of ferrocene in the temperature range of 333-1200 K (see **Scheme 1**). The reactions are assigned to Roman numbers, which will be used throughout the text to refer to the respective reaction. The colors of intermediates correspond to the data in **Figure 6**. Gray species are hypothetic intermediates, which were not detected by the i^{2}PEPICO experiment. The asterisk denotes products, which are probably adsorbed on the

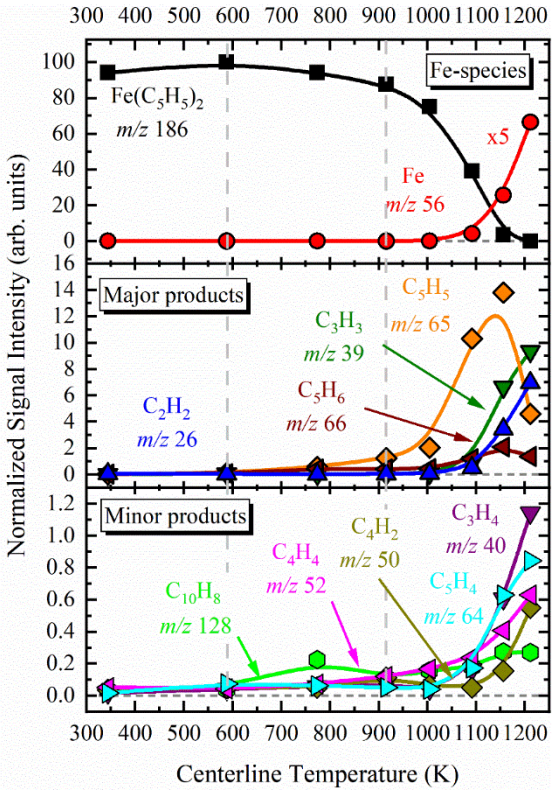

Figure 6 Temperature-dependent species profiles of products of thermal decomposition of $Fe(C_5H_5)_2$ at T_{vap} = 353 K (820 ppm), probed by i^{2}PEPICO VUV-mass spectrometry in our microreactor. The respective species that were characterized according to **Section 2.3** are labelled by their formula and all signals are normalized to the initial ferrocene signal.

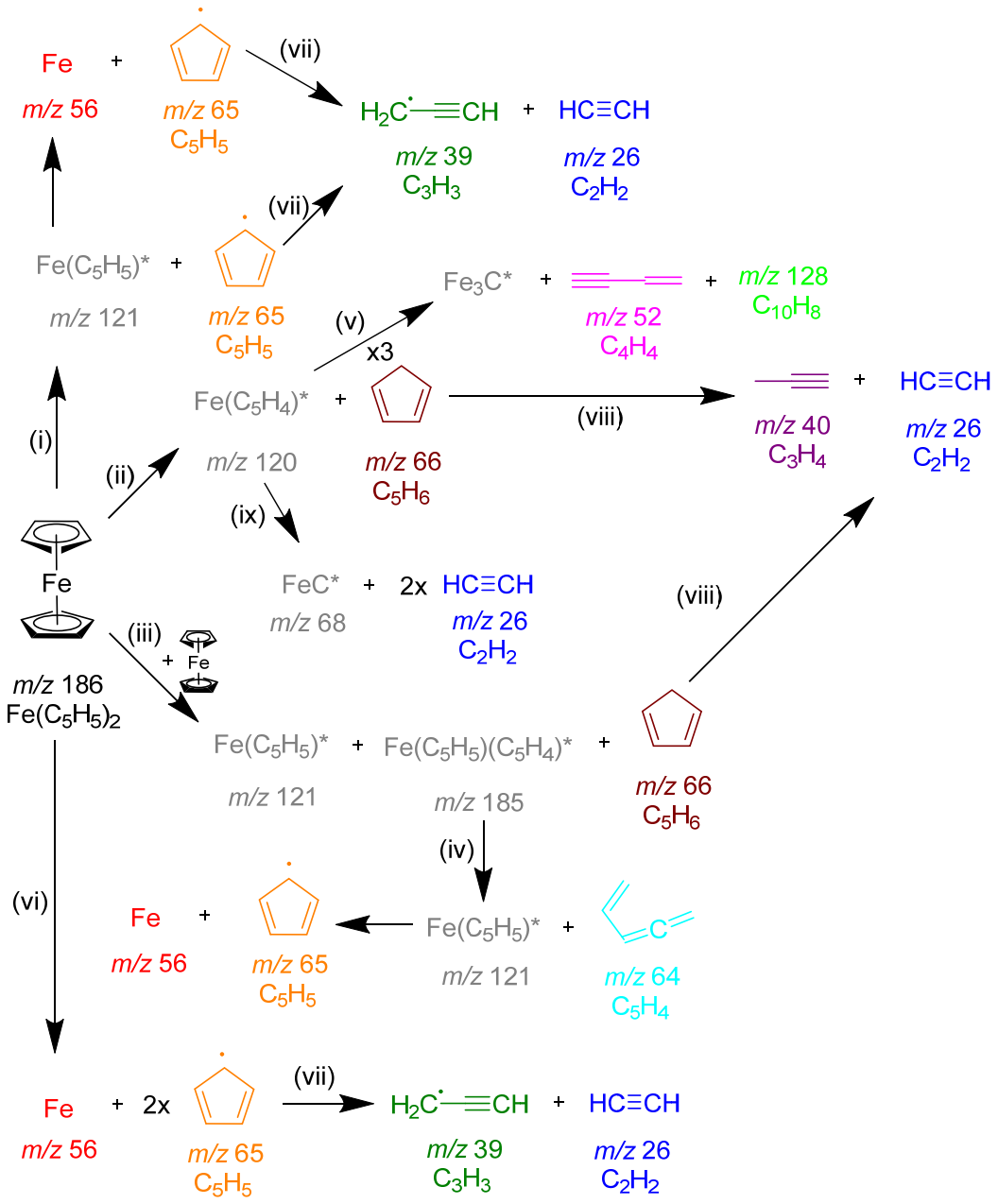

Scheme 1 Schematic reaction mechanism of the decomposition of $Fe(C_5H_5)_2$ in the gas-phase, which is rationalized by ms-TPE spectra and temperature-dependent species profiles. The colors of the species in the scheme correspond to their label in **Figure 6**. Gray species marked by an asterisk are hypothetic intermediates, which were not detected in the gas-phase by the i^{2}PEPICO experiment.

surface. Ferrocene already starts to decompose at 600 K but only above 900 K iron and hydrocarbon intermediates appear in significant amounts in the gas-phase. Consequently, three regimes can be distinguished in this experiment, for T < 600 K no reaction is observed, for T = 600-900 K ferrocene decomposition is initiated, while above 900 K gas-phase intermediates and atomic iron are formed. This behaviour was not expected from the literature data, which reports ferrocene to decompose in very low-pressure pyrolysis at around 1100-1200 K.[39,57] The temperature onset of ferrocene decomposition in this study agrees with the onset reported

by Dyagileva et al.[41] at around 673 K. Since their reactor is operated in batch mode (long residence time), it is expected that a considerable number of catalytic Fe-particles are produced, which reduce the decomposition temperature in their study. In contrast, in our study the high dilution in argon leads to a low number density of catalytic Fe-particles, which reduces the probability of catalytic surface reactions.

The species profiles in **Figure 6** reveal that for temperatures up to 1000 K, $Fe(C_5H_5)_2$ decomposes primarily via the loss of a cyclopentadienyl radical (*m/z* 65) leaving $Fe(C_5H_5)$ (*m/z* 121) (**Scheme 1**: reaction(i)). We postulate a second pathway of ferrocene decomposition, which may yield $Fe(C_5H_4)$ (*m/z* 120) and C_5H_6 based on the observation of cyclopentadiene below 1000 K (reaction (ii)). Neither atomic iron, nor other iron-containing intermediates were detected in the gas-phase at temperatures below 1000 K. If these species were formed in gas-phase reactions, we expect to be able to detect them based on previous experimental experience.[48] Additionally, previous studies of other investigators by quadrupole mass spectrometry also did not observe their formation at temperatures below 1173 K.[25] It is evident from the findings by Dyagileva et al.[43] that the activation energy for the thermolysis of the Fe-Cp bond on a surface is much lower than in the gas-phase. A similar behavior is observed in our study, because a significant amount of Fe is only detected in the gas-phase after heating the reactor above 1000 K, although ferrocene already decomposes at lower temperatures. We suggest that at temperatures < 1000 K, ferrocene undergoes decomposition in the gas-phase, forming cyclopentadienyl *m/z* 65 and cyclopentadiene *m/z* 66, followed by a very fast adsorption of the iron-containing species *m/z* 121 $Fe(C_5H_5)$ and *m/z* 120 $Fe(C_5H_4)$ on the surface of the reactor (see **Scheme 1** (i) and (ii)). Alternatively, ferrocene molecules react e.g. with other ferrocene molecules or iron containing reaction products from ferrocene on the surface under the liberation of cyclopentadiene according to reaction (iii):

$$2\ Fe(C_5H_5)_2{}^{*} \rightarrow Fe(C_5H_5)^{*} + Fe(C_5H_5)(C_5H_4)^{*} + C_5H_6 \qquad \text{(iii)}$$

Previous studies presented evidence that this may be a possible pathway for similar π-complexes of transition metals[40,80] under CVD conditions and that the unstable $Fe(C_5H_5)(C_5H_4)$***** radical decomposes on the surface to form the C_5H_4 species, which is also detected in our study (see **Figure. 5 (c)**) according to reaction (iv):

$$Fe(C_5H_5)(C_5H_4)^{*} \rightarrow Fe(C_5H_5)^{*} + C_5H_4 \qquad \text{(iv)}$$

The interpretation that surface reactions occur in the low temperature regime is further supported by the detection of $C_{10}H_8$ species such as 3-butene-1-ynylbenzene at *m/z* 128, while the naphthalene contributions were negligible (see **Figure 5 (d)**). Additionally, the low number density of C_5H_5 radicals in the sample precludes the recombination reaction in the gas-phase,[81] as also the dimer $C_{10}H_{10}$ is absent at any reactor temperature, which was found to be an intermediate to yield $C_{10}H_8$ species, recently.[82] Therefore we think it is likely that the species at *m/z* 128 forms on the surface by a reaction of neighboring iron-containing species. For example, $Fe(C_5H_4)$* molecules could form cementite (Fe_3C) as outlined in a previous study for the formation of iron thin films:[8]

$$3\ Fe(C_5H_4)^* \rightarrow Fe_3C^* + C_4H_4 + C_{10}H_8 \qquad \text{(v)}$$

Indeed, we observe C_4-species in the mass spectra, identified as vinylacetylene at *m/z* 52 (C_4H_4) at *m/z* 50 (see **Figure 5 (a)** and **(b)**) at temperatures below 1000 K, which may be formed in reaction (v). Those hydrocarbons may additionally form on the surface by a decomposition of benzyne (C_6H_4),[83] which may also partly explain the formation of *m/z* 128 at lower temperatures by a reaction with *m/z* 52 vinylacetylene under the liberation of H_2 to form *m/z* 128, 3-butene-1-ynylbenzene.

Only traces of benzene and toluene were detected, due to the generally low concentrations of the precursor and reaction products in the gas phase. Heavier aromatics than $C_{10}H_8$ were not observed and may remain on the surface and may contribute to an iron catalyzed CNT or soot growth, since we found black residue in the reactor after each experimental run. This interpretation is supported by the observation, that iron is generally capable of adsorbing or dissolving carbon.[14] Since the composition of the solid residue on the reactor wall is at best difficult to achieve in a microreactor and was therefore not analyzed, the formation of CNTs is speculative and will not be discussed further.

Compared to the low temperature decomposition pathways of ferrocene, the mechanism changes significantly at higher temperatures > 1000 K (see **Figure 6**). Following the species profiles in **Figure 6,** it is evident and commonly accepted in the literature,[57] that at T > 1000 K ferrocene decomposes in the gas-phase leading to the formation of two cyclopentadienyl radicals *m/z* 65 and atomic iron *m/z* 56 (**Scheme 1**: (vi)).[17] Both acetylene (C_2H_2) and the propargyl radicals (C_3H_3) are clearly observed in the ms-TPE spectra at temperatures above 1000 K (**Figure4 (a)** and **(b)**). The decrease in the *m/z* 65 signal intensity and a simultaneous increase of *m/z* 26 and 39, explains that these organic products are formed in secondary

reactions in the gas-phase (vii). Likewise it has been reported, that cyclopentadiene with *m/z* 66 decomposes to form propyne (*m/z* 40) and acetylene (*m/z* 26) (viii),[84] which were identified by their characteristic fingerprints utilizing ms-TPE spectra. Other experiments[8,40] revealed, that the pyrolysis of ferrocene at high temperatures, yields cementite (Fe_3C) and iron surrounded by graphite layers (FeC). The formation of FeC* can be rationalized by reaction (ix) of $Fe(C_5H_4)$* *m/z* 120 which may also contribute to the *m/z* 26 signal of acetylene observed here:

$$Fe(C_5H_4)^* \rightarrow FeC^* + 2\,C_2H_2 \qquad \text{(ix)}$$

The presence of acetylene in the gas-phase accelerates the formation of carbon coated iron nanoparticles or carbon nanotubes,[17,24] at particle forming conditions.[34]

2.5 Influence of H_2 addition

In comparison to the pyrolysis of pure ferrocene, higher signals for the masses *m/z* 26, 42, 43 and 44 were detected at temperatures below 1000 K if hydrogen is added to the reaction mixture (see **Figure 7 (a)**). We were able to identify the latter three signals as C_3 hydrocarbons according to their ionization onsets in the literature in comparison to our recorded threshold photoelectron spectra, as shown in **Figure. 7 (a)** and **(b)**. The shape of the ms-TPES in **Figure 7 (a)** is in agreement with the photoelectron spectrum of propene (C_3H_6) with a vertical ionization energy of 9.73 eV.[76] Based on the ionization onset at 10.9 eV, we assign the signal at *m/z* 44 to propane.[76] Unfortunately, we did not record spectra at photon energies higher than 11 eV, which would give a much clearer identification. The signal-to-noise ratio for the spectrum of *m/z* 43 is not shown here, because we did not record ms-TPE spectra at such low

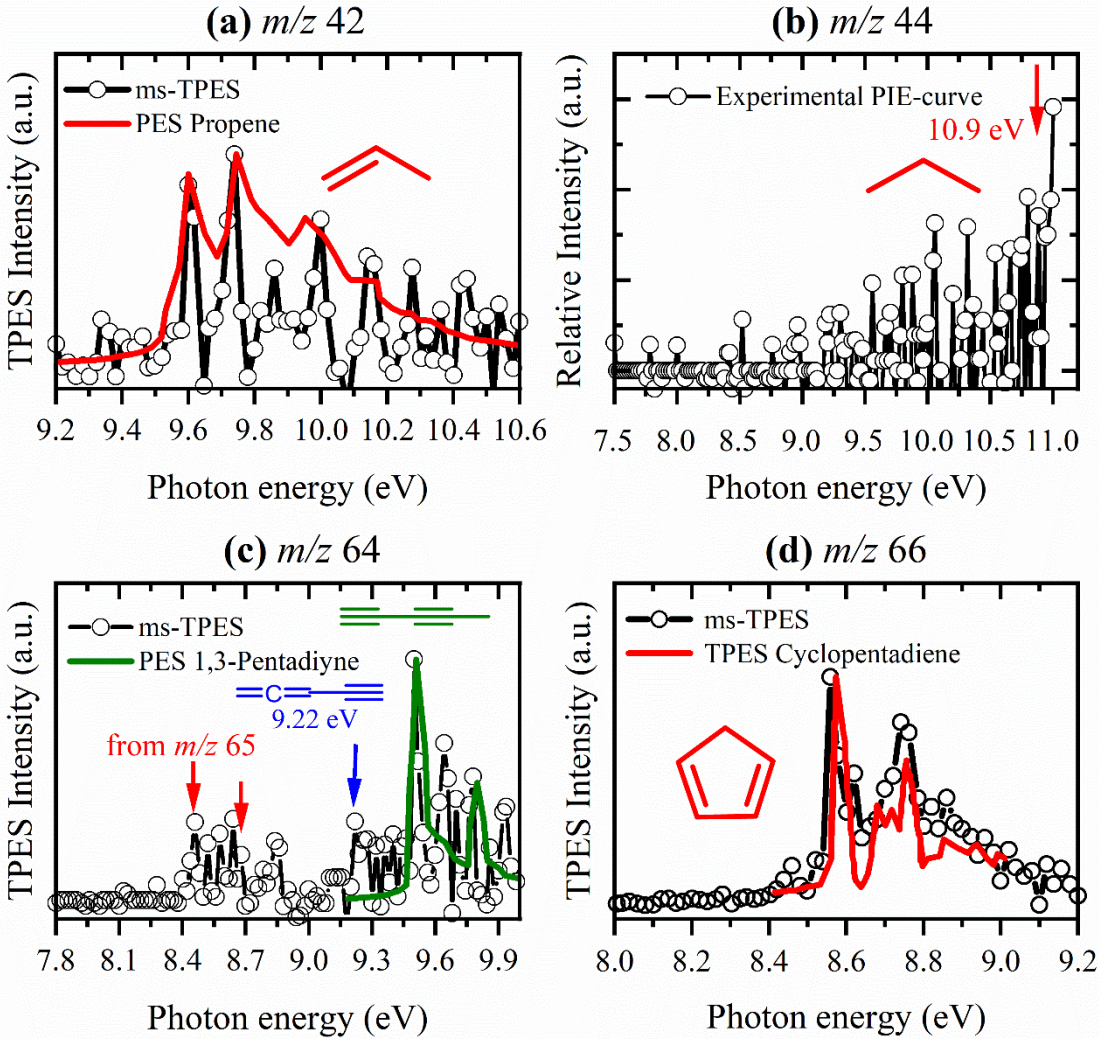

Figure 7 Representative examples of species identification and assignment of important decomposition products after adding 10% H_2 to the carrier gas flow, using experimental obtained TPE spectra (black dots and lines) **(a)**,(c)-**(d)** and PIE curves **(b)**. The species are either characterized by literature reference spectra (colored) , or by specific ionization onsets in **(b)** and **(c)**. References are as follows: **(a)** *m/z* 42 C_3H_6 (propene)[76], **(b)** *m/z* 44 C_3H_8 (propane)[76] **(c)** *m/z* 64 red: contribution from c-C_5H_5, blue: ethynylallene[69] and green: 1,3 pentadiyne[70]; **(d)** *m/z* 66 c-C_5H_6 (cyclopentadiene)[63].

temperatures, where the formation of *m/z* 43 can be observed. Yet, we tentatively assign this species to C_3H_7 according to a possible H-abstraction reaction of *m/z* 44 at temperatures higher than 600 K,[85] which is rationalized in the species profile on the lower part of **Figure 8**. The blend of the channel *m/z* 64 does change in comparison to pure pyrolysis (see **Figure 5 (c)**). Now ethynylallene (IE = 9.22 eV)[69] is also a spectral carrier of our signal, hinting at a change in the formation mechanism of C_5H_4 at temperatures above 1000 K. Since the signal of *m/z* 66 also increases in the presence of hydrogen, we checked this mass for additional isomers, but found exclusively cyclopentadiene, as can be seen in **Figure 7 (d)**.

It is evident from the data in **Figure 8 (left)** and **(right)** that the addition of H_2 leads to a decomposition of ferrocene at lower temperatures as compared to our measurements in argon (see **Figure 6**) and more hydrocarbon intermediates are observed. The decomposition temperature is shifted under these experimental conditions to a lower value of around 550 K in agreement with trends reported in the literature.[6] The exact temperature of the onset depends on the different reactor geometries and experimental conditions applied in both studies, but the general trend remains the same. Numerical simulations of the deployed microreactor in a

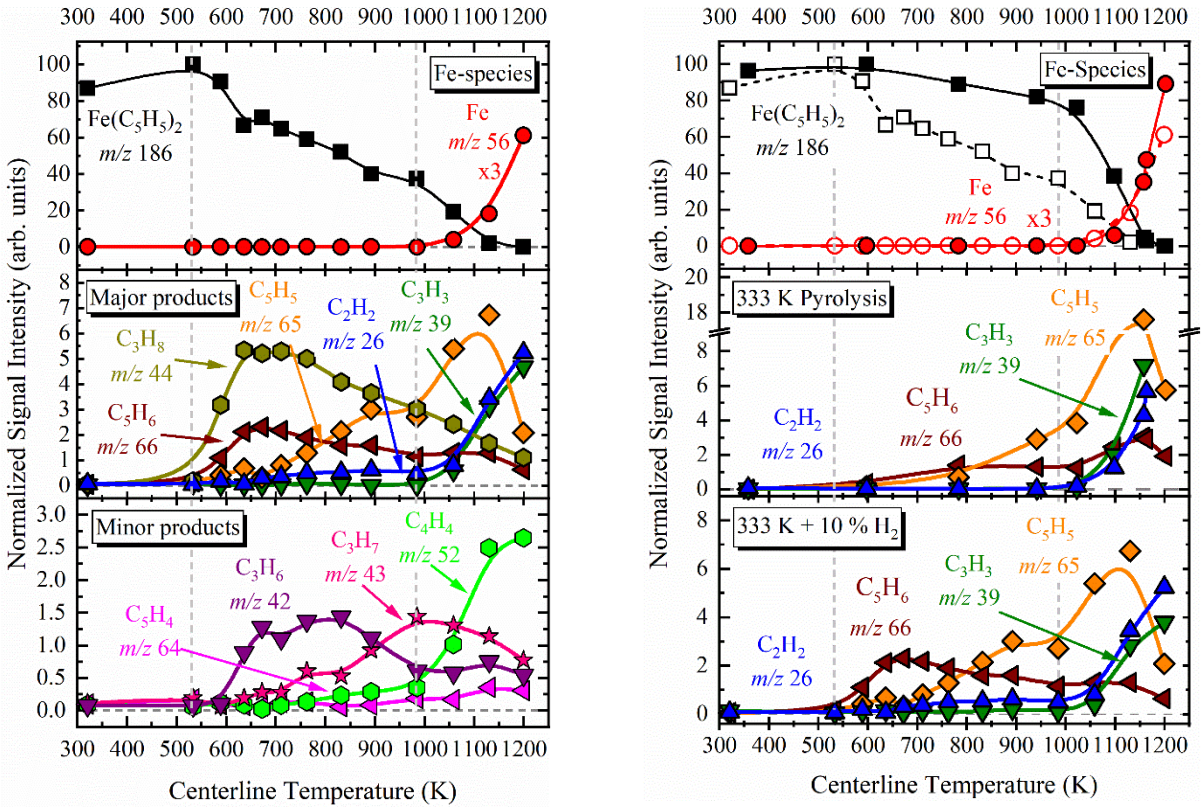

Figure 8 Left: Temperature-dependent species profiles of the most important intermediates and products observed during the reduction of 158 ppm ferrocene (T_{vap} = 333 K) with 10 % hydrogen. **Right:** Top trace: Comparison of the ion signal intensities with temperature of the iron species upon pyrolysis (filled symbols, straight lines) and the course of decomposition of ferrocene in reductive atmosphere (open symbols, dashed lines); Middle trace: Major pyrolysis products with an inlet concentration of 158 ppm ferrocene as a function of reactor temperature (Note: The y-axis contains a breakpoint from 8 to 18 in order to ensure comparability with the graph on the bottom trace.) ; Bottom trace: Major species upon addition of 10 % H_2. All species are labelled by their assigment.

previous study[48] revealed, that the average temperature is at least 6 % higher at the wall than on the centerline of the reactor, which brings us closer to the temperature value given in the literature.

Figure 8 (left) shows the temperature-dependent profiles of the intermediates formed during the decomposition of ferrocene in the presence of hydrogen. Below 1000 K the main hydrocarbon intermediates are 1,3-cyclopentadiene (c-C_5H_6), propene (C_3H_6) and propene (C_3H_8) and acetylene (C_2H_2), indicating that the underlying decomposition mechanism changes. In contrast to the measurement without H_2 addition the amount of C_5H_4 is reduced in the high temperature window. This observation is further rationalized by the steep signal increase of *m/z* 42, 44 and 65 in **Figure 8 (right)** starting at around 550 K. It can be assumed that direct reactions with hydrogen should explain this behavior of ferrocene and its decomposition products.

The reaction sequence of ferrocene reduction in the temperature window from 550 to 650 K may be initiated by a subsequent reaction starting from reaction (i) in the absence of H_2, which may take place in the gas-phase or on the surface by the following pathway:

$$Fe(C_5H_5)_2 \rightarrow Fe(C_5H_5)^* + C_5H_5 \rightarrow \quad \text{(Ia)}$$

$$Fe(C_5H_5)^* \rightarrow Fe(C_5H_5)^*(ads) \quad \text{(Ib)}$$

$$C_5H_5 + H_2 \rightarrow C_5H_5 + H \quad \text{(Ic)}$$

The C_5H_5 ligands are hydrogenated to form C_5H_6, which remains or subsequently desorbs into the gas-phase (Ic). This interpretation is supported by the increase of the C_5H_6 signal in **Figure 8 (right)** relative to C_5H_5, as compared to the pyrolysis without H_2 (see **Figure 6**). In addition to the H-radicals formed by reaction (Ic), hydrogen molecules are expected to dissociatively adsorb over iron on the surface of the reactor, which may lead to a lowering of the dissociation barrier of ferrocene upon hydrogen addition and decomposition.[46]

Previous experimental studies agree that the decomposition of c-C_5H_6 is initiated by C-H bond fission, leading to the formation of the cyclopentadienyl radical.[86] As already discussed in the light of reaction (viii), cyclopentadiene can additionally isomerize by hydrogen shifts and ring-opening and later breakdown to form C_2H_2 and C_3H_4 at higher temperatures.[65,84] This is in agreement with the development of the C_2H_2 and C_5H_6 signal at temperatures above 1000 K in the bottom trace of **Figure 8 (right).** However, these reaction channels do not explain the small acetylene signal below 1000 K, observed in the species profiles upon H_2 addition, in **Figure 8**

(right), which must have a different origin, though. It has been pointed out that the reduction of similar metallocenes, undergoes a competitive reaction mechanism between the hydrogenation of the ligands followed by metal bond cleavage and the decomposition of the ligands on the surface leading to carbon incorporation in the solid films and the formation of particles.[87] It is likely, that a similar mechanism takes place here, while hydrogen is present, as proposed by Russel et al. for the pure pyrolysis of ferrocene.[40] A surface hydrogenation followed by desorption of the hydrogenated ligands should not be dominant. Indeed, we found no evidence for C_5H_x (x = 8, 10) species in the gas-phase, which were proposed and observed by others for the hydrogenation of ligand radicals in ferrocene decomposition.[6],48 Possible reaction products from surface reactions of the postulated hydrogenated species may come from a rapid decomposition of C_5H_8 and C_5H_{10} on the surface or in the gas-phase followed by the formation of the products *m/z* 26 acetylene (C_2H_2), *m/z* 42 propene (C_3H_6) and *m/z* 44 propane (C_3H_8), for n = 1,2 respectively:

$$C_5H_6{}^* + nH_2 \rightarrow C_5H_{6+2n}{}^* \quad \text{(IIa)}$$

$$C_5H_{6+2n}{}^* \rightarrow C_3H_{10-2n}{}^* + C_2H_2{}^* \quad \text{(IIb)}$$

$$C_3H_{10-2n}{}^* \rightarrow C_3H_{10-2n} \quad \text{(IIc)}$$

$$C_2H_2{}^* \rightarrow C_2H_2 \quad \text{(IId)}$$

This explains, why we already observed acetylene in the sample in the initial stages of ferrocene decomposition. It is likely that *m/z* 43 belongs to C_3H_7 generated by the commonly known H-atom transfer reaction of C_3H_8 with H-radicals,[85] which are formed in excess by the initiation reaction sequence (Ic).

As already indicated, in comparison to the case without hydrogen addition, **Figure 8** reveals, that the formation of C_5H_4 is suppressed, since we observe almost no signal at *m/z* 64 in the low temperature regime. Since we only observe traces of ligand fragments and significant amounts of hydrogenated ligands, we conclude, that by addition of 10 % H_2, the hydrogenation reaction of C_5H_5 on the surface is dominant due to active H radicals, in comparison to the destruction of the C_5H_5 ligand radicals to smaller hydrocarbons. This should promote the formation of iron films with less carbon content, since the destruction of the ligands is necessary for the formation of pure carbon on the surface.[40] Instead H_2 purges the surface, leading to less carbon coverage, suppressing the formation of FeC and Fe_3C. This should lead to more active catalytic iron sites, which in turn enhances the decomposition of ferrocene by generating H-radicals from the decomposition of ferrocene and a possible contribution of hydrogen to the radical pool, as proposed by Luo and coworkers.[46]

If compared to the thermal decomposition in argon, significant amounts of C_4 hydrocarbons were also detected. Since the characterization of *m/z* 52 C_4H_4, as 1-buten-3-yne remains the same as in pyrolysis, we believe that this species is formed in a reaction similar to (ix). The detection of C_4H_2 can be attributed to either a methyl loss from cyclopentadiene to form C_4H_2 at higher temperatures and also a hydrogen loss of vinylacetylene, since we only observe 1,3 butadiene at temperatures higher than 1000 K (see **ESI Figure S3**).

2.6 Kinetics of the thermal decomposition of ferrocene

Since the flow field of our microreactor has been investigated numerically by CFD simulations in a previous study,[48] we are able to determine the residence time, temperature and pressure more precisely for various experimental boundary conditions. In the temperature window that applies to this study, an average pressure in the reactor of 1500 Pa and residence times between 26 and 44 µs were determined. Using this data, we can relate the mole fraction profiles (see **Figure 9 left**) of *m/z* 186, $Fe(C_5H_5)_2$ to the centerline temperature of the reactor.

Taking a closer look on **Figure 9 (left)** and considering the discussion about the reaction mechanism in the previous sections (**2.4**) and (**2.5**), we think that the ferrocene decomposition can be divided in two main channels. First, at low temperatures, we observe the surface reaction of ferrocene or its initial decomposition product, probably after adsorption, with first order kinetics according to:

$$Fe(C_5H_5)_2(g) \rightarrow Fe(C_5H_5)^*(ads) + Products \quad (2)$$

This is responsible for the decrease of the ferrocene mole fraction from ca. 300-950 K in **Figure 9 (left)**. Following the course of the mole fraction profiles, one recognizes a steep decrease in mole fraction near 1000 K hinting at a change in the dominant decomposition process in this temperature regime. Since we observe the formation of cyclopentadienyl radicals, as well as atomic iron in the gas-phase at these temperatures (see **Figure 6**), we assume that they are formed in the gas-phase according to the reaction **Equation 3** initially proposed by Lewis and Smith:[57]

$$Fe(C_5H_5)_2(g) \rightarrow Fe + 2 \cdot C_5H_5 \quad (3)$$

Reasonable Arrhenius plots were derived for the pyrolysis of $Fe(C_5H_5)_2$, with and without 10 % H_2, as shown in **Figure 9 (right)** and **Figure 10**, respectively. The process of data evaluation is described in paragraph **(4.1)** in detail. Briefly, the measured mole fractions at different

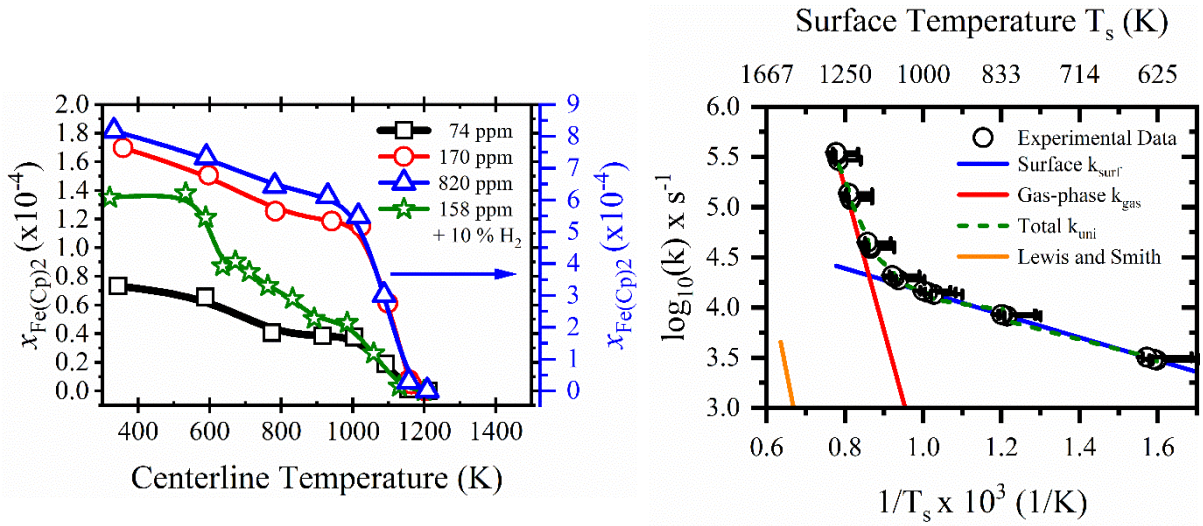

Figure 9 Left: Mole fraction profiles of $Fe(C_5H_5)_2$ (b-spline: curve, data: symbols) obtained with aid of CFD modelling at a computed average pressure of 1500 Pa and residence times from 26 to 44 µs for three initial ferrocene concentrations (74 ppm: black squares; 170 ppm: red circles; 820 ppm: blue triangles; 170 ppm; 158 ppm +10 % H_2: green stars). **Right:** Arrhenius plot (fit: colored curves, data: symbols) derived for the decomposition of $Fe(C_5H_5)_2$ at temperatures from ca. 300 to 1230 K. The range of activation energy of $Fe(C_5H_5)_2$ decomposition is given next to the plots. The error bars given in the right plot are based on the uncertainty in the determination of the decomposition temperature from surface temperature readings and CFD simulations.

temperatures and reaction times were used to fit the parameters of **Equation (9)**, in order to derive both activation energies and pre-exponential factors. All single fitting results combined with their validities are summarized in **Table 2**. To quantify the goodness of the fit of the activation energy, uncertainties are given next to the respective energies. Additionally, the sum of squared residuals (SSR) of the fits are registered in the last column. It has become apparent, that the goodness of fit is sensitive to the initial ferrocene concentration, since the signal intensities that underlie the mole fraction profiles are more concise.

We interpret the data as follows: Adsorption and subsequent surface reactions as **Equation (2)** dominate the temperature regime up to 900 K, where the conversion is relatively low. The activation energy in this regime is 21.9 kJ mol^{-1}. The kinetic parameters estimated by Hirasawa et al.[12] (A_0 = 1 x 10^7 s^{-1} E_a = 12.54 kJ mol^{-1}) using thermochemistry and quantum chemistry agrees fairly well with our low temperature activation energy, which we attribute to the existence of radicals and loosely bound H on the surface. The Arrhenius plots for the gas-phase decomposition according to **Equation (3)** in the temperature range from 330 to 1230 K are displayed in **Figure 10 (right)**. This is also the temperature regime where atomic iron and cyclopentadienyl radicals were detected as major primary decomposition products (see **Section 2.3**). Since at these high temperatures the depletion of $Fe(C_5H_5)_2$ is dominated by gas-phase reactions, we derived kinetic rate constants for the gas-phase reaction written in the bottom part of **Table 2**. Satisfactory fits to the data representing the high temperature gas-phase reaction lead to an activation energy range of $E_{a,g}$ = 272.3 kJ mol^{-1}, whereas the pre-exponential factor is determined to be 3.70 x 10^{16} s^{-1}. Earlier experimental determinations of the kinetic rate

coefficients differ largely from each other due to differences in experimental conditions and techniques. The bandwidth ranges from 171 kJ mol^{-1} in surface-catalyzed closed systems probed by EI-TOF,[41] over 209 kJ mol^{-1} under the impact of radicals in flames[88] to an activation energy of 382 kJ mol^{-1} attributed to the gas-phase reaction under very low-pressure pyrolysis determined by EI-TOF in a Knudsen cell.[57]

Table 2 Kinetic parameters for the thermal decomposition on the surface (top) and in the gas-phase (bottom) of $Fe(C_5H_5)_2$ in inert and reductive (10 % H_2) atmosphere.

Conditions T_{Range} [K]	A_0 [s^{-1}]	E_a [kJ mol^{-1}]	SSR [a.u.]
$Fe(C_5H_5)_2(g) \rightarrow Fe(C_5H_5)^*(ads) + Products$			
320-900	2.02 ± 0.41 x 10^5	21.9 ± 1.5	0.997
10% H_2/ 650-900	3.21 ± 0.94 x 10^5	18.9 ± 2.0	0.990
$Fe(C_5H_5)_2(g) \rightarrow Fe + 2 \cdot C_5H_5$			
> 900	3.70 ± 8.56 x 10^{16}	272.3 ± 22.9	0.997
10% H_2/ > 900	0.30 ± 3.65 x 10^{18}	286 ± 118	0.990

In our previous work we showed the presence of surface reactions which follow, as for other organometallic precursors, a Langmuir-surface catalyzed kinetics.[41] As discussed in the previous paragraph, the influence of H-radicals, emanating from the initial stages of the decomposition of ferrocene, as well as those that may be produced surface-catalyzed, explain the range in which the activation energy has been determined. The values obtained in this work are close to the ones measured for the radical interaction of 209 kJ mol^{-1} and the 171 kJ mol^{-1}, which take the influence of surface catalyzed kinetics into account. This is especially the case for the decomposition of ferrocene in the presence of hydrogen, since H_2 is present in excess and contributes significantly to the H-radical pool in our reactor. In contrast, earlier work by Lewis and Smith quotes an activation energy of 382 kJ mol^{-1}, which is significantly higher than the value obtained in our study. We attribute this discrepancy to the influence of surface reactions and H-radical formation on the surface as well as bimolecular reactions in the gas-phase of ferrocene with H_2 as in part already suggested by others for metallocenes.[41,43,80]

The influence of H_2 addition on the kinetics can be seen in the green curve of **Figure 9 (left)**, where the mole fraction of ferrocene in the hydrogen-rich atmosphere exhibits an earlier decrease at around 500 K compared to the pure pyrolysis. As already discussed in the previous

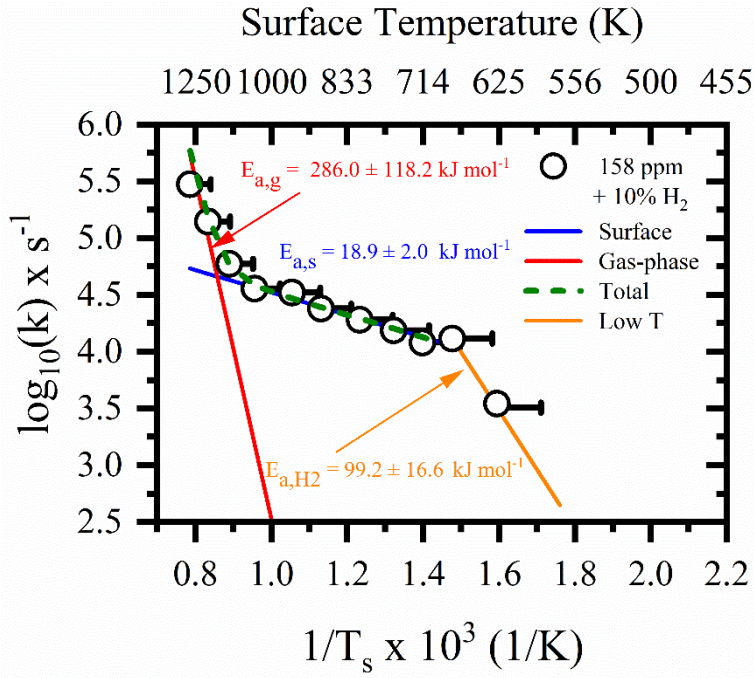

Figure 10 Arrhenius plot (fit: colored curves, data: symbols) derived for the decomposition of $Fe(C_5H_5)_2$ adding 10 % H_2 at an initial concentration of 1.58 x 10^{-4} (158 ppm) at temperatures from ca. 500 to 1250 K. The activation energy for the three reaction regimes are given next to the best fit plot (red: gas-phase, blue: surface, orange: reaction with H_2 on the surface). The influence of H_2 addition does play a large role at lower temperatures shown by the orange plot, where a reaction leads to the formation of C_3 -species in the gas-phase (see **Section 2.5**).

paragraph, we attribute this observation to a decomposition of hydrogenated ligands on the surface and a subsequent desorption of these hydrogenated species. From the Arrhenius plot in **Figure 10**, we can distinguish between two surface reaction regimes and obtain a pre-exponential factor of 9.93 10^{20} l mol^{-1} s^{-1} and an activation energy of 99.2 ± 16.6 kJ mol^{-1}, which are valid from 500-625 K. However, one should note, that considering the pyrolysis data in the temperature range from 500-900 K, we must consider that there is an overlap between both surface reactions, leading to an additional error in the reaction rate constants obtained in this study. Additionally, it is clear from **Figure 10** that our fit overestimates the gas-phase activation energy with a value of 268.2 kJ mol^{-1}. A reduction of these values may bring us closer to the energy of 218 kJ mol^{-1} proposed by Kuwana and Saito[33] for the global reaction:

$$Fe(C_5H_5)_2 + H_2 \rightarrow Fe + 2 \cdot C_5H_6 \qquad (4).$$

3. Conclusion

Sensitive, selective and multiplexed PEPICO spectroscopy was utilized with VUV synchrotron radiation to investigate the thermal decomposition of ferrocene in a hot microreactor with residence times < 100 μs in an inert or hydrogen atmosphere. It was demonstrated, that the thermal decomposition under these conditions can be mainly divided in two temperature regimes. At temperatures up to 900 K, surface reactions dominate, while at higher temperatures gas-phase reactions are faster. The first one involves the decomposition and adsorption of ferrocene or fragments as $Fe(C_5H_5)$ and $Fe(C_5H_4)$ on the surface, which are corroborated by the findings of cyclopentadienyl radicals and cyclopentadiene. The latter one includes the direct formation of atomic iron and cyclopentadienyl radicals in the gas-phase.

We showed, that other organic dissociation side products could be identified, such as *m/z* 26, 39, 50, 52 64 and 128. These were identified as acetylene, the propargyl radical, acyclic isomers of C_5H_4, as well as a mixture of naphthalene, 1-butene-3-ynylbenzene and 1-butene-3-ynylbenzene, respectively. The roles of these species in the reaction mechanism have been discussed. In the case of H_2 the reaction mechanism changes significantly, such that the decomposition products of ferrocene are either hydrogenated on the surface or directly react with hydrogen to form cyclopentadiene at temperatures < 900 K. In sum, new unimolecular dissociation channels could be identified from ferrocene (**Scheme 1**), which were not foreseen in previous studies, showing that limited experimental approaches due to fragmentation or longer residence times in the reactor might give an incomplete picture of the reaction sequences in ferrocene decomposition.

The kinetics of the two main decomposition channels were analyzed. Both reactions follow first order kinetics with a low activation energy of 21.9 kJ mol^{-1} for the surface reaction dominating the decomposition at low temperatures and 272.3 kJ mol^{-1} for the gas-phase decomposition, dominating the mechanism above 900 K. The decomposition mechanism changes significantly, when hydrogen is present in the reaction mixture. The hydrogenation of cyclopentadienyl ligands as well as their fragments is dominating in the ferrocene conversion. This leads to a reduction in the decomposition temperature in a probably bimolecular reaction of ferrocene with hydrogen at temperatures between 600 and 700 K, taking place in parallel to the above stated decomposition. The kinetics for the reaction with hydrogen were determined to have an activation energy of 18.9 kJ mol^{-1} at low temperatures. The latter should lead to reduced temperatures in iron CVD with hydrogen addition.

We have shown that our method is quite versatile, due to its capability of detecting highly reactive and elusive radicals and can be utilized to investigate the kinetics of further CVD

precursors. However, the kinetic studies should be complemented by investigations with traditional mass-spectrometric detection behind larger flow reactors, since the temperature profiles are easier to characterize, and the measurement times are less restricted. Hence, a combination of both methods should give an even deeper insight to the reactions of such organometallic precursors used for the synthesis of functional materials, which remain rare so far.

4. Experimental Section/ Methods

The experiments were conducted at the vacuum ultraviolet (VUV) beamline[89] at the Swiss Light Source of the Paul Scherrer Institute in Switzerland. A detailed description of the experimental apparatus[90,91], as well as the microreactor setup,[92] can be found elsewhere[48] and only a brief explanation is given here (see **Figure 11**). Ferrocene (> 98 % pure, Sigma Aldrich Inc.) is sublimed in a stainless-steel tube, jacketed by a copper block, to ensure isothermal sublimation conditions. Temperature and pressure of the sublimation source are continuously monitored and are constant during each measurement. Special attention was paid to reactor conditions that ensure primarily unimolecular dissociation. This is achieved by using a highly diluted sample stream, which minimizes the potential of bimolecular reactions. For this purpose, the precursor gas is diluted in a large excess of Argon (99.9999% purity), which is delivered by mass flow controllers (MKS Instruments) at a constant flow rate of 22 sccm. We conducted three separate experiments operating at an evaporator pressure of 1500 mbar and sublimation temperatures of 323/ 333/ 353 K. Assuming thermal equilibrium, the precursor mole fractions at the reactor inlet are calculated from the vapor pressure data[5] to be between $x_{Fe(C5H5)2} = 7.4\ 10^{-5}$ - $8.2\ 10^{-4}$. After sublimation, the mixture is expanded through a 100 µm pinhole into a resistively heated silicon-carbide (SiC)[93] flow reactor with an inner diameter of 1.0 mm and a heated length of 10 mm. To measure the decomposition temperature, a C-Type thermocouple with an estimated uncertainty in the examined temperature range between the centerline and surface temperature of ± 100 K. Under the conditions used here, residence times of 26-44 µs and an average pressure of 1500 Pa in

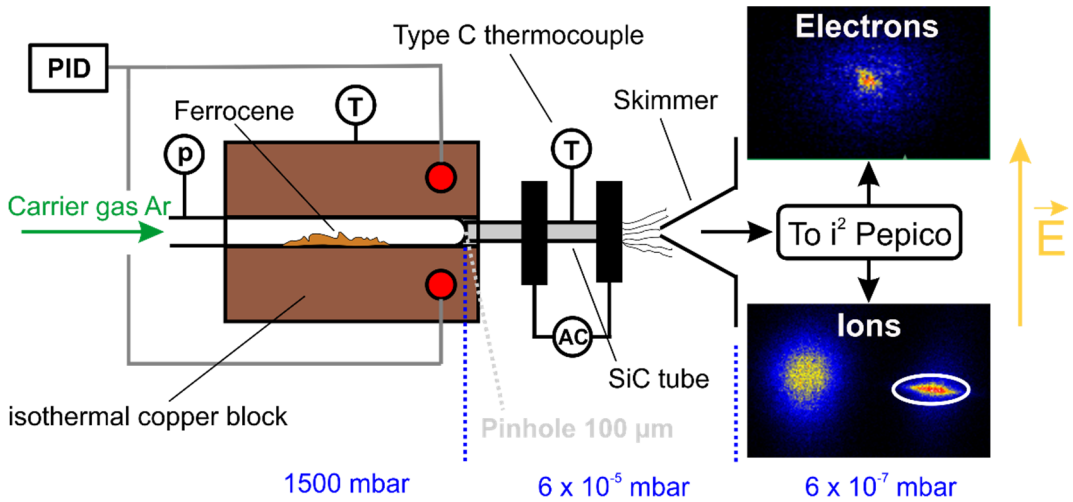

Figure 11 Schematic sketch of the evaporation source (brown) and the SiC pyrolysis reactor (gray) coupled to the i²PEPICO system. Exemplary electron (top) and ion (bottom) images are shown on the right hand side. The white ellipse on the velocity mapped (VMI) ion image, represents the region of interest chosen to sample the translationally cold molecular beam directly, suppressing the background and minimize the dissociative photoionization signal.

the microreactor were calculated.[48] A CFD simulation of the temperature field provided more realistic centerline temperatures, which were used in this study for the derivation of temperature-dependent species profiles. Since it is expected, that after a while, considerable amount of deposit may be formed on the reactor surface, we replaced the SiC-microreactor tube before conducting the experiments in reductive atmosphere. After the heated reaction zone, the decomposition products are rapidly expanded to high vacuum at ~ $6x10^{-5}$ mbar, leading to the formation of an effusive molecular beam that minimizes contact time, and preserves the actual gas composition including highly reactive species. The ejected gas is sampled by a nickel skimmer with a 2 mm orifice at the tip, which cuts the central part of the gas mixture, emitting a fractional part of the pyrolyzed gas towards the ionization chamber with a background pressure of < 10^{-6} mbar. Once the skimmer is passed, the molecules are irradiated with tunable, synchrotron radiation, dispersed by a VUV grating, perpendicularly hitting the ionization chamber with an energy resolution of 6 meV, leading, when absorbed, to the formation of photoions and photoelectrons, respectively. The cations and electrons are separated by applying a constant electric extraction field of 243 V cm^{-1}, which accelerates both in opposite directions. Incoming electrons and ions are subsequently detected in coincidence by two Roentdek DLD40 fast delay-line anode position-sensitive detectors at different impact radii that are proportional to their respective initial kinetic energy perpendicular to the extraction axis and the square root of the ion mass.[94] This photoelectron photoion coincidence (PEPICO) setup allows for selection of a region of interest in the VMI to distinguish direct ionization from dissociative ionization (see **Figure 11**, ion image). In all experiments, we either kept the photon energy constant at near-threshold photoionization energies of the decomposition species of interest or scanned the energy incrementally with a step size of 0.025 eV in the 7.8–11.7 eV range. Mass spectra for the decomposition products at 9.0, 10.5, 11.5, 14.2 and 15.8 eV were recorded within a temperature range from 333 K to 1250 K. For each species, we suppressed fragmentation by either staying below the threshold or selecting the ROI in the VMI. The recorded spectra allow us to derive temperature-dependent species profiles. During post-processing, all recorded threshold photoelectron spectra were corrected by the corresponding photon energy specific photon flux. Using these techniques allows to assign species by their molecular mass, photoionization (PIS) or their threshold photoelectron spectrum (TPE) with a resolution of ≤ 20 meV, which are corrected for hot electron contribution according to Sztáray et al.[95]. If compared to

Franck-Condon simulations or reference spectra, reactive intermediates (radicals, carbenes) and stable molecules can be isomer-selectively detected.[55,58] Adiabatic ionization energies and bond dissociation energies were calculated using different DFT methods (B3LYP, M06L, ωb97xd) at the 6-311++G(d,p) basis set, as implemented in the Gaussian 16 suit of programs.[96] The given values for the appearance ionization energy (AIE) are corrected for the respective zero-point energies.

Kinetics

As we demonstrated in a previous study for aluminum acetylacetonate,[48] the utilization of comprehensive numerical simulations of the flow field in the microreactor enables us to determine kinetic parameters of the primary decomposition step. For the sake of clarity the reader is referred to our work on the numerical simulation of the microreactor, which is described in detail elsewhere.[48]

In brief, to determine the temperature dependence of the $Fe(C_5H_5)_2$ mole fraction, we follow the procedure proposed by Zhang et al.,[97] where the influence of temperature-dependent signal variations of argon (*m/z* 40) due to a change in expansion behavior and therefore the sampling efficiency is characterized by the gas expansion coefficient $\lambda(T)$. We determined this expansion coefficient by recording temperature-dependent mass spectra at fixed photon energy of 15.8 eV in the 300-1300 K range (see **ESI: Figure S4**). The correlation between the mole fraction of ferrocene at temperature T to the mole fraction at T_0 at an incident photon energy of 9.0 eV and a fixed photon flux is given as follows:

$$c_{Fe(C_5H_5)_2}(T) = c_{Fe(C_5H_5)_2}(T_0) \cdot \lambda(T) \cdot \frac{S_{Fe(C_5H_5)_2}(T)}{S_{Fe(C_5H_5)_2}(T_0)} \qquad (5)$$

,where $S_i(T)$ represents the ion signal intensity measured at temperature T and $c_{Fe(C_5H_5)_2}$ is defined as the precursor concentration measured at temperature T. The gas expansion factor is unity at room temperature. As a starting point, the inlet mole fraction was calculated assuming saturated conditions inside the evaporator; for an evaporation temperature of 323/ 333 and 353 K, respectively. This results in $x_{Fe(C_5H_5)_2}(T_0)$ = 7.4 × 10^{-5} to 8.2 x 10^{-4} from previously measured vapor pressure data by our group.[5] Given this, reasonable Arrhenius plots were derived using the integral method for the unimolecular dissociation reaction of ferrocene (see **Section 2.6**). Since unimolecular gas-phase dissociation reactions of metal-organic precursors often follow first order kinetics, which was also determined here experimentally, the rate constant was approximated using the Arrhenius law shown in **Equation (6)**:

$$k_{uni}(T) = A_0 \cdot \exp\left(\frac{E_a}{RT}\right) \quad (6)$$

, where A_0 represents the collision frequency and E_a the molar activation energy in kJ mol^{-1}. This holds for gas-phase and for surface reactions, but the pre-exponential factor and the activation energies differ. The time dependent concentration change for a unimolecular reaction is given by:

$$\frac{dc}{d\tau} = -k_{uni}(T) \cdot c \quad (7).$$

Separation of variables, integration of **Equation (7)** and combination with **Equation (6)** yields:

$$\mathrm{c}(\tau) = \mathrm{c}(\tau_0) \cdot \exp\left[-A_0 \cdot \exp\left(\frac{E_a}{RT}\right) \cdot (\tau - \tau_0)\right] \quad (8)$$

Taking the natural logarithm gives:

$$\ln\left(\frac{\mathrm{c}(\tau)}{\mathrm{c}(\tau_0)}\right) = -\mathrm{k_{uni}}(\tau - \tau_0) \quad (9).$$

Since surface and gas-phase reactions take place concurrently in our microreactor, the total rate constant is the sum of both contributions. Since both rate constants follow the Arrhenius expression given in **(6)** we derived them simultaneously according to **Equation (10)**:

$$k_{uni}(T) = k_{gas}(T) + k_{surf}(T) \quad (10)$$

The experimental data $\mathrm{c}(\mathrm{c_0}, \mathrm{T}, \tau)$ is then fitted to **Equation (9)**, which results using **Equation (6)** in the unknown kinetic parameters A_0 and E_a for the homogeneous and the heterogeneous reaction, respectively. Earlier experiments using metallocenes by others let us conclude, that this is also the case for surface reactions following the Langmuir–Hinshelwood mechanism, which is first order at low partial pressures of $Fe(C_5H_5)_2$.[41]

In the case of ferrocene mixed with H_2, one might expect a bimolecular reaction, with its reaction being second order. Since hydrogen is present in excess in the reaction mixture and the concentration of ferrocene does not exceed 820 ppm, the reaction of ferrocene with hydrogen can be approximated as pseudo-first order leading to a similar Arrhenius expression as in **Equation (6)**:

$$k_{eff}(T) = A_{0,H_2} \exp\left(\frac{E_{a,H_2}}{RT}\right) \quad (11)$$

Following the procedure, described above, also pseudo-first order rate constants for ferrocene in 10% hydrogen have been determined, which is discussed in **Section 2.6** in more detail.

Supporting Information

Supporting Information is available from the xxx or from the author.

CRediT authorship contribution statement

S. Grimm: investigation, formal analysis, visualization, writing – original draft; P. Hemberger: investigation, resources, writing – review & editing; T. Kasper: conceptualization, methodology, supervision, writing – review & editing, project administration, funding acquisition; B. Atakan: conceptualization, methodology, supervision, writing – review & editing, project administration, funding acquisition.

Declaration of Competing Interest

The authors declare that they have no known competing financial interests or personal relationships that could have appeared to influence the work reported in this paper.

Acknowledgements

The authors gratefully acknowledge Andras Bodi, Sascha Lau, Dennis Kaczmarek and Thomas Bierkandt for experimental research support. All authors thank the German Research Foundation (DFG) for financial support under contract 399583933. The measurements have been performed at the VUV beamline of the Swiss Light Source, at the Paul Scherrer Institute in Villigen, Switzerland.

Received: ((will be filled in by the editorial staff))
Revised: ((will be filled in by the editorial staff))
Published online: ((will be filled in by the editorial staff))

Using a soft ionization method coupled to velocity map imaging (VMI), leads to valuable insights in the thermal decomposition of an exemplary organometallic precursor, $Fe(C_5H_5)_2$, used in the synthesis of functional nanomaterials and iron oxide coatings. Thanks to the use of a microreactor, important gas-phase species with a short lifetime are observed and assigned upon pyrolysis.

Sebastian Grimm[a,c], Patrick Hemberger[b], Tina Kasper[c,d], Burak Atakan[a,d]*

Mechanism and kinetics of the thermal decomposition of $Fe(C_5H_5)_2$ in inert and reductive atmosphere: A synchrotron-assisted investigation in a microreactor

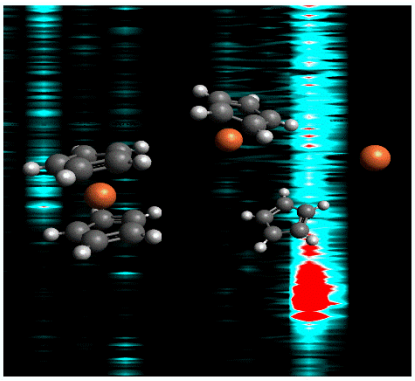

Supporting Information

Mechanism and kinetics of the thermal decomposition of $Fe(C_5H_5)_2$ in inert and reductive atmosphere: A synchrotron-assisted investigation in a microreactor

Sebastian Grimm[a,c]*, *Patrick Hemberger*[b], *Tina Kasper*[b,c], *Burak Atakan*[a,c]

[a] IVG, Institute for Combustion and Gas Dynamics – Mass Spectrometry in Reacting Flows, University of Duisburg-Essen, 47057, Germany
[b] Laboratory for Synchrotron Radiation and Femtochemistry, Paul Scherrer Institute, CH-5232 Villigen-PSI, Switzerlandd
[c] IVG, Institute for Combustion and Gas Dynamics – Mass Spectrometry in Reacting Flows, University of Duisburg-Essen, 47057, Germany
[d] CENIDE, Center for Nanointegration Duisburg-Essen, University of Duisburg-Essen, 47057, Germany

E-mail address: sebastian.grimm@uni-due.de (S. Grimm)

S1: VMI-image of focused molecular beam

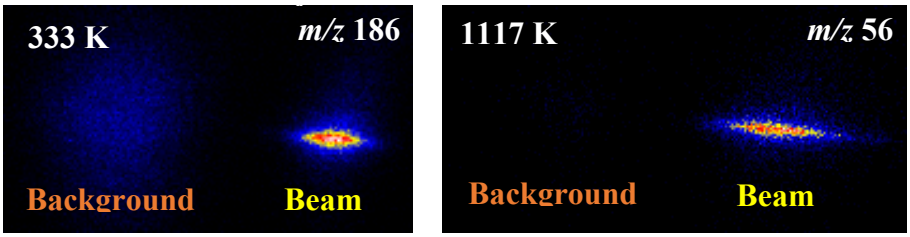

Figure S 1: Ion images of a molecular beam at a photon energy of 9 eV recorded by velocity map imaging (VMI). The specific images of the mass channels are displayed, which belong to the precursor ferrocene (*m/z* 186) **(left)** at 333 K and atomic iron (**right**), as a major decomposition product on *m/z* 56 at 1117 K. The narrow kinetic energy distribution, represented by a narrow beam component, can easily be identified, which adds an additional analytical dimension. This enables us to unequivocally distinguish between dissociative and direct ionized species.

S2: Origin of impurity cyclopentadienone (*m/z* 80)

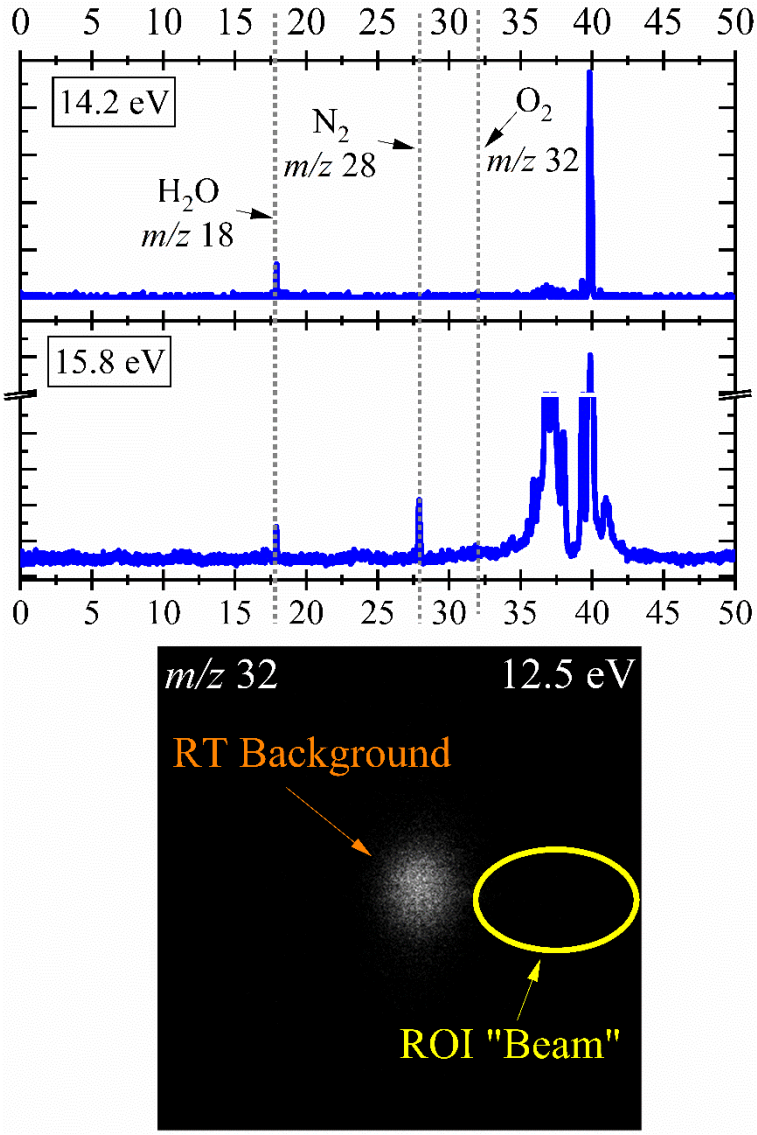

Figure S 2 Top: Exemplary mass spectra at 14.2 and 15.8 eV in order to identify possible signals of water (IE = 12.62 eV), nitrogen (IE = 15.58 eV) and oxygen (IE = 12.07 eV).[67] **Bottom:** Velocity map images of ions from an exemplary measurement at a photon energy of 12.5 eV, which only consider the mass channel *m/z* 32; orange denotes the room temperature background, thus no signal from the sample, yellow denotes the region of interest (ROI) for the molecular beam component. Since almost no ions are observable in the beam, we conclude, that the contribution of oxygen impurity in the sample is at most very low.

Here we briefly discuss the origin of the signal at *m/z* 80 in our mass spectra at 11.5 eV in **Figure 2** of the main text. This peak is assigned to cyclopentadienone. Since we did not add oxygen as reactive gas in our experiments, this species is considered to be an impurity. Small amounts of 1-butene-3-yne may also stem from a decarbonylation of cyclopentadienone.[98] One source could be O atoms attached to the walls of the reactor or the solid sample in the evaporator, another could be small traces of O_2 in the gas sample by small amounts of solvents (e.g. ethanol) that are used for cleaning the evaporator after each experiment. Nevertheless, we

believe that our results are not affected by the oxygen contamination (see ion image in **Figure S2**), since the amount of oxygen in the gas sample is relatively low in comparison to the signal intensity of ferrocene. In addition, the ionization cross section of cyclopentadienone at 10.5 eV is approximately three times larger than the one for the cyclopentadienyl radical.[66] As a result, the absolute concentration of *m/z* 80 is significantly smaller than the concentrations of the major pyrolysis products.

S3: Threshold photoelectron spectrum of *m/z* 54 at 1079 K

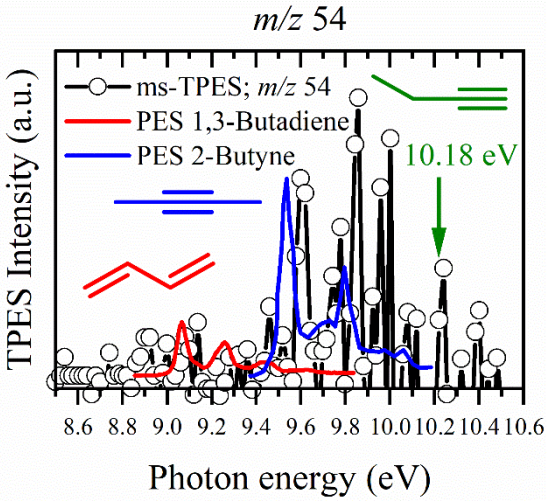

Figure S 3 ms-TPES of mass channel 54 along with their assignment to the following C_4H_6 isomers by literature references; red: 1,3-butadiene[78], blue: 2-butyne[77], green: 1-butyne[67].

S4: Temperature-dependent gas expansion factor λ

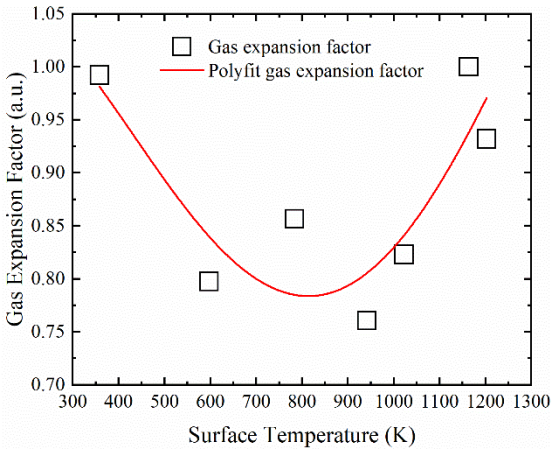

Figure S 4 Gas expansion factor as a function of surface temperature.

References:

[1] T. J. Kealy, P. L. Pauson, *Nature* **1951**, *168*, 1039.
[2] S. A. Miller, J. A. Tebboth, J. F. Tremaine, *J. Chem. Soc.* **1952**.
[3] D. Astruc, *Eur. J. Inorg. Chem.* **2017**, *2017*, 6.
[4] H. Werner, *Angewandte Chemie (International ed. in English)* **2012**, *51*, 6052.
[5] S. Lau, B. Atakan, *J. Chem. Eng. Data* **2020**, *65*, 1211.
[6] G.J.M. Dormans, *Journal of Crystal Growth* **1991**, *108*, 806.
[7] M. Mukaida, I. Hiyama, T. Tsunoda, Y. Imai, *Thin Solid Films* **2001**, *381*, 214.
[8] F. Senocq, F.-D. Duminica, F. Maury, T. Delsol, C. Vahlas, *Surface and Coatings Technology* **2006**, *153*, G1025.
[9] T. Gao, C. Zhou, Y. Zhang, Z. Jin, H. Yuan, D. Xiao, *J. Mater. Chem. A* **2018**, *6*, 21577.
[10] X. Liu, X. Liang, H. Lou, H. Wang, H. Li, S. Zhang, S. Zhu, W. Han, B. Zhou, *Sustainable Energy Fuels* **2021**, *5*, 1067.
[11] A. E. Elwardany, M. N. Marei, Y. Eldrainy, R. M. Ali, M. Ismail, M. M. El-kassaby, *Fuel* **2020**, *270*, 117574.
[12] T. Hirasawa, C.-J. Sung, Z. Yang, A. Joshi, H. Wang, *Combustion and Flame* **2004**, *139*, 288.
[13] S. Huang, R. Yang, J. Wang, S. Chang, X. Gou, C. Hua, J. Zhao, *J Heterocyclic Chem* **2020**, *57*, 2854.
[14] D. R. Chen, M. Chitranshi, M. Schulz, V. Shanov, *Nano LIFE* **2019**, *09*, 1930002.
[15] H. W. Zhu, C. L. Xu, D. H. Wu, B. Q. Wei, R. Vajtai, P. M. Ajayan, *Science (New York, N.Y.)* **2002**, *296*, 884.
[16] A. Moisala, A. G. Nasibulin, D. P. Brown, H. Jiang, L. Khriachtchev, E. I. Kauppinen, *Chemical Engineering Science* **2006**, *61*, 4393.
[17] Y. Xu, Y. Ma, Y. Liu, S. Feng, D. He, P. Haghi-Ashtiani, A. Dichiara, L. Zimmer, J. Bai, *J. Phys. Chem. C* **2018**, *122*, 6437.
[18] M. D. Yadav, A. W. Patwardhan, J. B. Joshi, K. Dasgupta, *Chemical Engineering Journal* **2019**, *377*, 119895.
[19] V. Y. Iakovlev, D. V. Krasnikov, E. M. Khabushev, A. A. Alekseeva, A. K. Grebenko, A. P. Tsapenko, B. Y. Zabelich, J. V. Kolodiazhnaia, A. G. Nasibulin, *Chemical Engineering Journal* **2020**, *383*, 123073.
[20] E. M. Khabushev, D. V. Krasnikov, J. V. Kolodiazhnaia, A. V. Bubis, A. G. Nasibulin, *Carbon* **2020**, *161*, 712.
[21] S. Zghal, I. Jedidi, M. Cretin, S. Cerneaux, M. Abdelmouleh, *Diamond and Related Materials* **2020**, *101*, 107557.
[22] M. D. Yadav, K. Dasgupta, *Ind. Eng. Chem. Res.* **2021**, *60*, 2187.
[23] A. Barreiro, S. Hampel, M. H. Rümmeli, C. Kramberger, A. Grüneis, K. Biedermann, A. Leonhardt, T. Gemming, B. Büchner, A. Bachtold, T. Pichler, *The Journal of Physical Chemistry B* **2006**, *110*, 20973.
[24] R. Bhatia, V. Prasad, *Solid State Communications* **2010**, *150*, 311.
[25] D. Lysenkov, J. Engstler, A. Dangwal, A. Popp, G. Müller, J. J. Schneider, V. M. Janardhanan, O. Deutschmann, P. Strauch, V. Ebert, J. Wolfrum, *Small (Weinheim an der Bergstrasse, Germany)* **2007**, *3*, 974.
[26] A. Leonhardt, S. Hampel, C. Müller, I. Mönch, R. Koseva, M. Ritschel, D. Elefant, K. Biedermann, B. Büchner, *Chem. Vap. Deposition* **2006**, *12*, 380.
[27] P. Lassègue, L. Noé, M. Monthioux, B. Caussat, *Phys. Status Solidi C* **2015**, *12*, 861.
[28] T. Gao, C. Zhou, Y. Zhang, Z. Jin, H. Yuan, D. Xiao, *J. Mater. Chem. A* **2018**, *6*, 21577.
[29] A. Peña, J. Puerta, A. Guerrero, E. Cañizales, J. L. Brito, *Journal of Nanotechnology* **2012**, *2012*, 1.

[30] S. A. Rashid, M. Z. A. Rashid, M. A. Musa, S. H. Othman, *Asia-Pac. J. Chem. Eng.* **2013**, *8*, 254.
[31] M. D. Yadav, K. Dasgupta, A. W. Patwardhan, A. Kaushal, J. B. Joshi, *Chemical Engineering Science* **2019**, *196*, 91.
[32] K. Kuwana, K. Saito, *Carbon* **2005**, *43*, 2088.
[33] K. Kuwana, K. Saito, *Proceedings of the Combustion Institute* **2007**, *31*, 1857.
[34] D. He, H. Li, J. Bai, *Carbon* **2011**, *49*, 5359.
[35] S. I. Futko, B. G. Shulitskii, V. A. Labunov, E. M. Ermolaeva, *J Eng Phys Thermophy* **2015**, *88*, 1432.
[36] S. Y. Moon, W. S. Kim, C. S. Kim, *RSC Adv.* **2018**, *8*, 25815.
[37] W. Ren, F. Li, S. Bai, H.-M. Cheng, *Journal of nanoscience and nanotechnology* **2006**, *6*, 1339.
[38] C. Liu, H.-M. Cheng, *Materials Today* **2013**, *16*, 19.
[39] P. J. Zandstra, *The Journal of chemical physics* **1964**, *40*, 612.
[40] D. K. Russell, *Chem. Vap. Deposition* **1996**, *2*, 223.
[41] L. M. Dyagileva, V. P. Mar'in, E. I. Tsyganova, G. A. Razuvaev, *Journal of Organometallic Chemistry* **1979**, *175*, 63.
[42] K. Elihn, K. Larsson, *Thin Solid Films* **2004**, *458*, 325.
[43] L. M. Dyagileva, E. I. Tsyganova, Y. A. Aleksandrov, *Russ. Chem. Rev.* **1988**, *57*, 316.
[44] T. Yamada, A. Maigne, M. Yudasaka, K. Mizuno, D. N. Futaba, M. Yumura, S. Lijima, K. Hata, *Nano letters* **2008**, *8*, 4288.
[45] W. Wasel, K. Kuwana, P. T.A. Reilly, K. Saito, *Carbon* **2007**, *45*, 833.
[46] J.-H. Luo, R.-Y. Luo, W.-G. Zhang, *Chem. Vap. Deposition* **2007**, *13*, 574.
[47] A. Bodi, P. Hemberger, D. L. Osborn, B. Sztáray, *J. Phys. Chem. Lett.* **2013**, *4*, 2948.
[48] S. Grimm, S.-J. Baik, P. Hemberger, A. Bodi, A. M. Kempf, T. Kasper, B. Atakan, *Physical chemistry chemical physics PCCP* **2021**, *23*, 15059.
[49] P. Schissel, D. J. McAdoo, E. Hedaya, D. W. McNeil, *The Journal of chemical physics* **1968**, *49*, 5061.
[50] A. Révész, L. Szepes, T. Baer, B. Sztáray, *Journal of the American Chemical Society* **2010**, *132*, 17795.
[51] J. Wang, L. Sheng, Y. Zhang, *Chinese Journal of Chemical Physics* **2004**, *17(2)*, 121-125.
[52] S. Liang, P. Hemberger, N. M. Neisius, A. Bodi, H. Grützmacher, J. Levalois-Grützmacher, S. Gaan, *Chemistry (Weinheim an der Bergstrasse, Germany)* **2015**, *21*, 1073.
[53] A. K. Vasiliou, K. M. Piech, B. Reed, X. Zhang, M. R. Nimlos, M. Ahmed, A. Golan, O. Kostko, D. L. Osborn, D. E. David, K. N. Urness, J. W. Daily, J. F. Stanton, G. B. Ellison, *The Journal of chemical physics* **2012**, *137*, 164308.
[54] S.-J. Han, M.C. Yang, C.H. Hwang, D.H. Woo, J.R. Hahn, H. Kang, Y. Chung, *International Journal of Mass Spectrometry* **1998**, *181*, 59.
[55] P. Hemberger, J. A. van Bokhoven, J. Pérez-Ramírez, A. Bodi, *Catal. Sci. Technol.* **2020**, *10*, 1975.
[56] B. Sztáray, A. Bodi, T. Baer, *Journal of mass spectrometry JMS* **2010**, *45*, 1233.
[57] K. E. Lewis, G. P. Smith, *J. Am. Chem. Soc.* **1984**, *106*, 4650.
[58] P. Hemberger, A. Bodi, T. Bierkandt, M. Köhler, D. Kaczmarek, T. Kasper, *Energy Fuels* **2021**, *35*, 16265.
[59] P. Hemberger, V. B. F. Custodis, A. Bodi, T. Gerber, J. A. van Bokhoven, *Nature communications* **2017**, *8*, 15946.
[60] J. M. Dyke, B. W. J. Gravenor, R. A. Lewis, A. Morris, *Molecular Physics* **1982**, *15*, 4523.

[61] P. Hemberger, G. da Silva, A. J. Trevitt, T. Gerber, A. Bodi, *Physical chemistry chemical physics PCCP* **2015**, *17*, 30076.
[62] T. A. Cool, J. Wang, K. Nakajima, C. A. Taatjes, A. Mcllroy, *International Journal of Mass Spectrometry* **2005**, *247*, 18.
[63] P. Hemberger, M. Lang, B. Noller, I. Fischer, C. Alcaraz, B. K. Cunha de Miranda, G. A. Garcia, H. Soldi-Lose, *The journal of physical chemistry. A* **2011**, *115*, 2225.
[64] J. Bouwman, A. Bodi, J. Oomens, P. Hemberger, *Physical chemistry chemical physics PCCP* **2015**, *17*, 20508.
[65] M. Gerlach, A. Bodi, P. Hemberger, *Physical chemistry chemical physics PCCP* **2019**, *21*, 19480.
[66] P. J. Linstrom, W. G. Mallard (Eds.), *NIST Chemistry WebBook, NIST Standard Reference Database 69*, National Institute of Standards and Technology, Gaithersburg MD, 20899.
[67] C. Baker, D. W. Turner, *Proc. R. Soc. Lond. A* **1968**, *308*, 19.
[68] F. Brogli, E. Heilbronner, J. Wirz, E. Kloster-Jensen, R. G. Bergman, K. P. C. Vollhardt, A. J. Ashe, *Helv. Chim. Acta* **1975**, *58*, 2620.
[69] N. Hansen, S. J. Klippenstein, J. A. Miller, J. Wang, T. A. Cool, M. E. Law, P. R. Westmoreland, T. Kasper, K. Kohse-Höinghaus, *The journal of physical chemistry. A* **2006**, *110*, 4376.
[70] F. Brogli, E. Heilbronner, V. Hornung, E. Kloster-Jensen, *Helv. Chim. Acta* **1973**, *56*, 2171.
[71] P. M. Mayer, V. Blanchet, C. Joblin, *The Journal of chemical physics* **2011**, *134*, 244312.
[72] Z. Pan, A. Puente-Urbina, A. Bodi, J. A. van Bokhoven, P. Hemberger, *Chemical science* **2021**, *12*, 3161.
[73] B. K. Cunha de Miranda, C. Alcaraz, M. Elhanine, B. Noller, P. Hemberger, I. Fischer, G. A. Garcia, H. Soldi-Lose, B. Gans, L. A. V. Mendes, S. Boyé-Péronne, S. Douin, J. Zabka, P. Botschwina, *The journal of physical chemistry. A* **2010**, *114*, 4818.
[74] B. Yang, J. Wang, T. A. Cool, N. Hansen, S. Skeen, D. L. Osborn, *International Journal of Mass Spectrometry* **2012**, *309*, 118.
[75] J. Krüger, G. A. Garcia, D. Felsmann, K. Moshammer, A. Lackner, A. Brockhinke, L. Nahon, K. Kohse-Höinghaus, *Physical chemistry chemical physics PCCP* **2014**, *16*, 22791.
[76] G. Bieri, F. Burger, E. Heilbronner, J. P. Maier, *Helv. Chim. Acta* **1977**, *60*, 2213.
[77] P. Masclet, G. Mouvier, J. F. Bocquet, *J. Chim. Phys.* **1981**, *78*, 99.
[78] T. K. Ormond, P. Hemberger, T. P. Troy, M. Ahmed, J. F. Stanton, G. B. Ellison, *Molecular Physics* **2015**, *113*, 2350.
[79] R. Gleiter, M. C. Bohm, R. D. Ernst, *Journal of Electron Spectroscopy and Related Phenomena* **1984**, *33*, 269.
[80] L. Brissonneau, R. Sahnoun, C. Mijoule, C. Vahlas, *J. Electrochem. Soc.* **2000**, *147*, 1443.
[81] A. E. Long, S. S. Merchant, A. G. Vandeputte, H.-H. Carstensen, A. J. Vervust, G. B. Marin, K. M. van Geem, W. H. Green, *Combustion and Flame* **2018**, *187*, 247.
[82] Z. Pan, A. Puente-Urbina, A. Bodi, J. A. van Bokhoven, P. Hemberger, *Chemical science* **2021**, *12*, 3161.
[83] W.-Q. Deng, K.-L. Han, J.-P. Zhan, G.-Z. He, *Chemical Physics Letters* **1998**, *288*, 33.
[84] C. Cavallotti, D. Polino, A. Frassoldati, E. Ranzi, *The Journal of Physical Chemistry A* **2012**, *116*, 3313.
[85] A. Lifshitz, M. Frenklach, *J. Phys. Chem.* **1975**, *79*, 686.
[86] I. V. Tokmakov, L. V. Moskaleva, M. C. Lin, *Int. J. Chem. Kinet.* **2004**, *36*, 139.
[87] L. Brissonneau, A. Reynes, C. Vahlas, *Chem. Vap. Deposition* **1999**, *5*, 281.

[88] G. T. Linteris, M. D. Rumminger, V. Babushok, W. Tsang, *Proceedings of the Combustion Institute* **2000**, *28*, 2965.
[89] M. Johnson, A. Bodi, L. Schulz, T. Gerber, *Nuclear Instruments and Methods in Physics Research Section A: Accelerators, Spectrometers, Detectors and Associated Equipment* **2009**, *610*, 597.
[90] B. Sztáray, K. Voronova, K. G. Torma, K. J. Covert, A. Bodi, P. Hemberger, T. Gerber, D. L. Osborn, *The Journal of chemical physics* **2017**, *147*, 13944.
[91] A. Bodi, P. Hemberger, T. Gerber, B. Sztáray, *The Review of scientific instruments* **2012**, *83*, 83105.
[92] P. Chen, S. D. Colson, W. A. Chupka, J. A. Berson, *J. Phys. Chem.* **1986**, *90*, 2319.
[93] D. W. Kohn, H. Clauberg, P. Chen, *Review of Scientific Instruments* **1992**, *63*, 4003.
[94] T. Baer, R. P. Tuckett, *Physical chemistry chemical physics PCCP* **2017**, *19*, 9698.
[95] B. Sztáray, T. Baer, *Review of Scientific Instruments* **2003**, *74*, 3763.
[96] M. J. Frisch, G. W. Trucks, H. B. Schlegel, G. E. Scuseria, M. A. Robb, J. R. Cheeseman, G. Scalmani, V. Barone, G. A. Petersson, H. Nakatsuji, X. Li, M. Caricato, A. V. Marenich, J. Bloino, B. G. Janesko, R. Gomperts, B. Mennucci, H. P. Hratchian, J. V. Ortiz, A. F. Izmaylov, J. L. Sonnenberg, D. Williams-Young, F. Ding, F. Lipparini, F. Egidi, J. Goings, B. Peng, A. Petrone, T. Henderson, D. Ranasinghe, V. G. Zakrzewski, J. Gao, N. Rega, G. Zheng, W. Liang, M. Hada, M. Ehara, K. Toyota, R. Fukuda, J. Hasegawa, M. Ishida, T. Nakajima, Y. Honda, O. Kitao, H. Nakai, T. Vreven, K. Throssell, Montgomery, Jr., J. A., J. E. Peralta, F. Ogliaro, M. J. Bearpark, J. J. Heyd, E. N. Brothers, K. N. Kudin, V. N. Staroverov, T. A. Keith, R. Kobayashi, J. Normand, K. Raghavachari, A. P. Rendell, J. C. Burant, S. S. Iyengar, J. Tomasi, M. Cossi, J. M. Millam, M. Klene, C. Adamo, R. Cammi, J. W. Ochterski, R. L. Martin, K. Morokuma, O. Farkas, J. B. Foresman, D. J. Fox, *Gaussian 16 Revision A.03* **2016**.
[97] T. Zhang, J. Wang, T. Yuan, X. Hong, L. Zhang, F. Qi, *The journal of physical chemistry. A* **2008**, *112*, 10487.
[98] T. K. Ormond, A. M. Scheer, M. R. Nimlos, D. J. Robichaud, T. P. Troy, M. Ahmed, J. W. Daily, T. L. Nguyen, J. F. Stanton, G. B. Ellison, *The journal of physical chemistry. A* **2015**, *119*, 7222.